Rhyolitic volcano dynamics in the Southern Andes: Contributions from 17 years of InSAR observations at Cordón Caulle volcano from 2003 to 2020

Francisco Delgado

Journal Pre-proof

Rhyolitic volcano dynamics in the Southern Andes: Contributions from 17 years of InSAR observations at Cordón Caulle from 2003 to 2020

Francisco Delgado

PII: S0895-9811(20)30384-9

DOI: https://doi.org/10.1016/j.jsames.2020.102841

Reference: SAMES 102841

To appear in: *Journal of South American Earth Sciences*

Received Date: 24 March 2020

Revised Date: 10 August 2020

Accepted Date: 21 August 2020

Please cite this article as: Delgado, F., Rhyolitic volcano dynamics in the Southern Andes: Contributions from 17 years of InSAR observations at Cordón Caulle from 2003 to 2020, *Journal of South American Earth Sciences* (2020), doi: https://doi.org/10.1016/j.jsames.2020.102841.

Rhyolitic volcano dynamics in the Southern Andes: contributions from 17 years of InSAR observations at Cordón Caulle from 2003 to 2020

Francisco Delgado [1]

[1]Université de Paris, Institut de Physique du Globe de Paris, CNRS, F-75005 Paris, France

[1]delgado@ipgp.fr

Abstract

In this article I present a review of InSAR observations of ground deformation at Cordón Caulle volcano, whose 2011-2012 VEI 4-5 eruption is the best scientifically observed and instrumentally recorded rhyolitic eruption to date. I document a complete cycle of pre-eruptive uplift, co-eruptive subsidence and post-eruptive uplift with InSAR data between March 2003 and May 2020 and produced by a complex interplay of magmatic processes. Pre-eruptive data show ∼0.5 m of ground uplift in three distinct episodes between 2003 and 2011, with uplift rates between ∼3 and ∼30 cm/yr. The uplift was likely caused by magma injection resulting in pressurization of the magmatic system at depths of 4-9 km. Data spanning the first 3 days of the eruption show ∼1.5 m of deflation produced by two distinct sources at 4-6 km depth located 18 km from each other and up to 10 km from the eruptive vent — suggesting hydraulic connectivity of a large magma mush zone. A third source of deformation was recorded during the rest of the eruption at a depth of ∼ 5 km, resulting in a total subsidence of ∼2.5 m. On a much smaller spatial scale (∼25 km^2), InSAR-derived digital elevation models recorded ∼250 m of uplift in the area of the eruptive vent interpreted as the intrusion of a shallow laccolith during the first 2.5 months of the eruption and time averaged lava discharge rates up to ∼150 m^3/s.The co-eruptive time series of reservoir pressure drop and extruded volume follow exponential trends that can be explained by a model of magma reservoir depressurizationand conduit flow. Since the end of the eruption, the surface of the volcano was uplifted ∼1 m in a sequence of three transient episodes of unrest during 2012 and 2019, with uplift rates between 6 and 45 cm/yr and lasting between 0.5 and 3.2 years. These pulses can be modeled by the same source, a sub-horizontal sill at a depth of ∼6 km. Viscoelastic relaxation is not significant on these time scales, hence I interpret these uplift signals as being produced by episodic pulses of magma injection in the crystal mush that likely underlies the volcano. The episodic and abrupt changes of the ground deformation suggests a restless trans-lateral magmatic system at depths of 4-9 km and active across multiple spatial and temporal scales. Finally, I also discuss challenges of the InSAR technology that should be addressed to detect ground deformation on short time scales, particularly under the low coherence conditions of Cordón Caulle.

1 Introduction

Volcanic eruptions are one of the most spectacular geological processes observed on Earth. These events are produced by the ascent and extrusion of magma, molten rock composed of melt, crystals, and gases. The occurrence, duration, and style (either explosive or effusive) of the resulting eruption depend on a complex interplay of factors. These include the magma volume, ascent rate, composition, volatile content, and physicochemical transformations that the magma undergoes as it ascends and depressurizes, traveling from its storage area in a shallow reservoir through either a narrow conduit or a sill to the surface (*Wilson et al.*, 1980; *Tait et al.*, 1989; *Jaupart and Tait*, 1990; *Jaupart*, 2000; *Edmonds and Wallace*, 2017; *Tait and Taisne*, 2012; *Dufek et al.*, 2012; *Gonnermann and Manga*, 2012; *Gonnermann*, 2015). The complexity of volcanic processes has been recently highlighted by a review article which stated that the first grand challenge in volcano science is to *"forecast the onset, size, duration, and hazard of eruptions by integrating observations with quantitative models of magma dynamics"* (*National Academies of Sciences and Medicine*, 2017). Fortunately, eruptions and/or the emplacement of magma in the upper crust are typically preceded by several signs of unrest including changes in ground deformation (e.g., *Pinel et al.*, 2014), temperature (*Reath et al.*, 2019), seismicity (e.g., *Chouet and Matoza*, 2013), and degassing (e.g., *Carn et al.*, 2016) that can provide insights into their dynamics, and potentially forecast them (*Sparks et al.*, 2012). However, there are still basic volcanological questions that remain unanswered. These include: 1. How is magma stored and transported in the crust? 2. What triggers eruptions? 3. What controls the duration and magnitude of eruptions? 4. What unrest signals are evidence of an imminent eruption? (*National Academies of Sciences and Medicine*, 2017; *Wilson*, 2017). Even in the best monitored volcanoes on Earth, eruption forecasting can be very challenging (*Thelen et al.*, 2017; *Peltier et al.*, 2018). Our understanding of the dynamics of these systems is still incomplete because we are inherently limited by the low resolving power of observations made from the Earth's surface (*Bachmann and Huber*, 2016) rather than in the actual reservoirs where magma is stored (*Lowenstern et al.*, 2017).

Ground deformation data is a useful tool for volcano monitoring because the ascent of magma and the resulting eruption are usually coeval with displacement on the Earth's surface (*Sparks et al.*, 2012). Thereby deformation allows us to potentially forecast and better understand volcanic processes. Volcano geodesy has traditionally relied on ground measurements including including tiltmeters and continuous GPS but it has been revolutionized by Interferometric Synthetic Aperture Radar (InSAR), providing new insights on a variety of volcanic processes like eruption dynamics (*Dzurisin and Lu*, 2007; *Pinel et al.*, 2014; *Lu and Dzurisin*, 2014; *Dumont et al.*, 2018; *Dzurisin et al.*, 2019). The key advantage of InSAR is that it is the only geodetic method that can measure ground deformation over large areas ($>$ 40x40 km^2) with repeat periods of a few days and with small uncertainties ($\sim$5 cm per interferogram). Compilations of satellite observations show a wide diversity of InSAR-derived deformation signals on volcanoes in Latin America (*Reath et al.*, 2019) and elsewhere (e.g., *Lu and Dzurisin*, 2014), but the relation between deformation and eruption is not always clear (*Biggs et al.*, 2014; *Biggs and Pritchard*, 2017; *Delgado et al.*, 2017; *Reath et al.*, 2019).

In this review article I present a summary of 17 years of InSAR observations at Cordón Caulle volcano (Figure 1) in the Southern Volcanic Zone (SVZ) of the Chilean and Argentinian Andes (*Stern*, 2004) and the magmatic processes that can be unravelled with InSAR observations. Although InSAR data have contributed to key observations of volcanic processes in the SVZ, particularly during the VEI4-5 2008-2009 Chaitén (*Wicks et al.*, 2011) and 2015 Calbuco (*Nikkhoo et al.*, 2016; *Delgado et al.*, 2017) eruptions and a sequence of unrest at Laguna del Maule volcano (*Feigl et al.*, 2014; *Le Mével et al.*, 2015; *Novoa et al.*, 2019), in no other volcano in the SVZ than at Cordón Caulle it has shed light about a wide variety of volcanic processes (*Pritchard and Simons*, 2004; *Fournier et al.*, 2010; *Jay et al.*, 2014; *Bignami et al.*, 2014; *Delgado et al.*, 2016, 2018, 2019; *Castro et al.*, 2016; *Wendt et al.*, 2017; *Euillades et al.*, 2017). These include a sequence of transient pre-eruptive pulses of magma injection, co-eruptive subsidence, lava flow extrusion and shallow laccolith intrusion, lava flow subsidence, and episodic post-eruptive magma injection that can lead to a potential new eruption (Figure 2). At the time of writing (July 2020), no other subduction volcano in America except for Okmok in the Aleutians (*Lu and Dzurisin*, 2014) displays the wide variety of signals due to magmatic and superficial processes that can be observed with InSAR. The discovery of ground deformation at Cordón Caulle has been directly related to improvements in the SAR civilian platforms. Therefore, in this review I rely on multiplatform InSAR data and relate them to other geological observations (*Castro et al.*, 2013, 2016; *Bonadonna et al.*, 2015) only when they are relevant for the scope of this study.

I start this review with a summary of InSAR and volcano geodesy studies in the Southern Andes, highlighting the value of the method with respect to other geodetic techniques, particularly for the scope of this special issue on **New advances on SAR Interferometry in South America**. I then describe a complete cycle of pre-eruptive uplift, co-eruptive subsidence and post-eruptive uplift at Cordón Caulle imaged with InSAR. Then, I describe volcanological aspects where InSAR has made a leap forward in our understanding of rhyolitic dynamics. I finalize with a discussion on the challenges and opportunities for a better use of InSAR in the Southern Andes, including a qualitative comparison of different SAR data sets for the environmental conditions of Cordón Caulle. The time period of this study starts in March 2003 and ends in January 2020. It spans since the beginning of the operation phase of ENVISAT which was the first platform to systematically acquire data in the area to the current COSMO-SkyMED, TerraSAR-X, Sentinel-1, ALOS-2 and RADARSAT-2 acquiring several hundreds of SAR images per year. Therefore, significant changes in the InSAR technology have resulted in a much faster discovery and better understanding of magmatic processes than before.

2 Volcano Geodesy in the Southern Andes

The Southern Volcanic Zone (SVZ) (Figure 1) is one of the most active volcanic segments in the Andean volcanic arc of South America (*Stern*, 2004) with a time-averaged eruption rate of ∼0.5 events/year during the 20th century (*Dzierma and Wehrmann*, 2012). The rate increased to ∼1.3 events/year between 2008 and 2016 (Llaima January 01 2008, Chaitén May 02 2008-2009, Llaima April 03 2009, Cordón Caulle 04 June 201, Peteroa 2010-2011, Hudson October 26 2011, Copahue December 2012, Villarrica 03 March 2015, Calbuco April 22 2015, Nevados de Chillan January 2016 - ongoing). These volcanoes have a wide range of eruptive styles that vary from small basaltic Strombolian (VEI 1-2) to large rhyolitic Plinian (VEI 5) eruptions. The SVZ includes Villarrica and Llaima, two of the most active edifices in South America with each having more than 50 historical eruptions since the mid XVI century. Of the 9 SVZ volcanoes that erupted during 2008-2017, Chaitén, Cordón Caulle, Villarrica and Calbuco are scientifically important regardless of their magma composition. The VEI 4-5 2008-2009 Chaitéen and 2011-2012 Cordón Caulle eruptions were the first and second rhyolitic eruptions with scientific instrumental observations in real time (*Major and Lara* 2013; *Jay et al.* 2014), the latter the first time that the extrusion of a rhyolitic lava flow has been observed in detail (*Tuffen et al.*, 2013). Villarrica is a basaltic/andesitic volcano that hosts one of the seven semi-permanent lava lakes on earth (*Lev et al.*, 2019). Finally, the VEI 4 2015 Calbuco eruption is a rare case of a sub-Plinian andesitic eruption with little to none geodetic and seismic precursory activity (*Delgado et al.*, 2017). The SVZ is thus an excellent place to constrain the mechanisms responsible for magma storage and transport, as well as to investigate how eruptions are triggered and evolve.

InSAR data have been recorded in the SVZ since 1993 (*Pritchard and Simons*, 2004), but systematic observations with good interferometric coherence have only been available since January 2007 by ALOS-1 data (*Fournier et al.*, 2010). InSAR provided the first geodetic observations in the SVZ volcanoes because to my knowledge classical ground geodesy such as tiltmeters and leveling were never attempted in this region. Several InSAR studies have been carried out in the SVZ including regional surveys (*Pritchard and Simons*, 2004; *Fournier et al.*, 2010; *Pritchard et al.*, 2013; *Delgado et al.*, 2017; *Reath et al.*, 2019) and detailed studies focused on individual volcanoes. These include from N to S Peteroa (*Romero et al.*, 2020), Laguna del Maule (*Feigl et al.*, 2014; *Le Mével et al.*, 2015, 2016; *Novoa et al.*, 2019; *Zhan et al.*, 2019), Domuyo (*Astort et al.*, 2019; *Lundgren et al.*, 2020), Nevados de Chillán (*Pritchard et al.*, 2013; *Reath et al.*, 2019; *Delgado*, 2018), Copahue (*Velez et al.*, 2011, 2015; *Lundgren et al.*, 2017; *Reath et al.*, 2019), Lonquimay (*Fournier et al.*, 2010), Llaima (*Fournier et al.*, 2010; *Bathke et al.*, 2011; *Remy et al.*, 2015; *Delgado et al.*, 2017), Villarrica (*Delgado et al.*, 2017; *Reath et al.*, 2019), Cordón Caulle (*Jay et al.*, 2014; *Bignami et al.*, 2014; *Delgado et al.*, 2016, 2018, 2019; *Wendt et al.*, 2017; *Euillades et al.*, 2017), Calbuco (*Nikkhoo et al.*, 2016; *Delgado et al.*, 2017), Chaitén (*Fournier et al.*, 2010; *Wicks et al.*, 2011;

Reath et al., 2019) and Hudson (*Pritchard and Simons*, 2004; *Delgado et al.*, 2014; *Reath et al.*, 2019). These studies show that the SVZ volcanoes have in general shallow magma reservoirs (z < 10 km), with injection rates of ∼0.01-0.03 km^3/yr. Some of these reservoirs are significantly offset from the center of the volcano (*Delgado et al.*, 2017). In some cases deformation preceded eruptions, while in some it did not (*Reath et al.*, 2019). The 2008-2009 Chaitén, 2011-2012 Cordón Caulle and 2015 Calbuco VEI 4-5 eruptions all were coeval with ground subsidence due to magma extraction from shallow reservoirs.

The large number of eruptions and the discovery of deforming volcanoes with InSAR in the past 12 years led to the deployment of continuous GPS and tilt meters for continuous monitoring in several volcanoes of the SVZ by OVDAS (Observatorio Volcanológico de los Andes del Sur), part of the Chilean Volcano Monitoring Network operated by SERNAGEOMIN (Servicio Nacional de Geología y Minería). The first permanent continuous GPS stations in the SVZ were deployed in October 2011 - February 2012 and in December 2017 for Cordón Caulle. Nevertheless, the late deployment of these instruments with respect to the eruptions and episodes of unrest implies that only in a few cases they have contributed to a better understanding of volcano dynamics in the SVZ with respect to InSAR (e.g., *Le Mével et al.*, 2015). Further, no permanent GPS stations existed at the time of the Chaitén, Cordón Caulle and Calbuco eruptions. Stations were deployed after the onset of the Chaitén (*Pina-Gauthier et al.*, 2013) and Cordón Caulle eruptions (*Wendt et al.*, 2017), and a single tiltmeter recorded the 2015 Calbuco eruption (*Delgado et al.*, 2017). However, the few data and the large distance with respect to the volcanoes required to interpret the data jointly with the InSAR observations. Finally, microgravity has only been recorded at Laguna del Maule volcano (*Miller et al.*, 2017), with an ongoing continuous microgravity deployment at the summit of Villarrica volcano (Héléne Le Mével, personal communication).

3 Cordón Caulle Geological Background

Cordón Caulle is a long-lived system made up of a graben bounded by two sets of NW-SE trending fissures and the central volcano of a NW-SE volcanic range made up by Cordillera Nevada caldera to the NW and Puyehue volcano to the SE (Figure 1, *Lara et al.*, 2004, 2006a,b). These three volcanoes have chemically distinct evolutions, with Cordón Caulle erupting only rhyolitic and rhyodacitic lavas in the Holocene (*Singer et al.*, 2008). The lava flows erupted in 1921-1922 and 1960 were sourced from vents located in the S fissure (*Lara et al.*, 2004; *Singer et al.*, 2008) and are rhyodacites and rhyolites respectively, with their rare earth element patterns overlapping suggesting a common magma source (*Castro et al.*, 2013). The VEI 4 1960 eruption occurred 1.5 days after the 1960 M_w 9.5 Valdivia megathrust earthquake suggesting a link between the two (*Barrientos*, 1994; *Lara et al.*, 2004).

The 2011-2012 eruption of Cordón Caulle (Figure 1) started on June 4, 2011 lasting for ∼9 months until March 2012, and was the first eruption of the volcano since 1960. The eruption was preceded by significant ground uplift between 2007 and 2011 (*Jay et al.*, 2014) and by 2 months of seismicity above background levels (*Wendt et al.*, 2017; *Delgado et al.*, 2018). The eruptive vent was located on the northern scarp that bounds the graben structure (Figure 1). The climactic phase of the eruption lasted ∼27 hours and ejected a ∼9-12 km high eruptive column, with a VEI of 4-5 with a mass flow rate (MFR) of $\sim 10^7$ kg/s, which then decreased to $\sim 10^6$ kg/s (*Bonadonna et al.*, 2015). The eruption style shifted from purely explosive to hybrid explosive–effusive on June 15, with the extrusion of ∼0.6 km^3 of a rhyolitic lava flow (*Coppola et al.*, 2017, Figure 1) punctuated by mixed ash-gas jets with Vulcanian blasts (*Schipper et al.*, 2013; *Castro et al.*, 2014) with MFR $<\sim 10^6$ kg/s, and correlated with an increase in the quasi-harmonic tremor (*Bertin et al.*, 2015). The lava time averaged discharge rate (TADR) decreased exponentially from the onset of extrusion until October-November 2011 (*Coppola et al.*, 2017), when a second pulse of lava effusion increased both the quasi-harmonic tremor and TADR until the eruption ended in March 2012 (*Bertin et al.*, 2015; *Coppola et al.*, 2017). A shallow laccolith with a volume of ∼0.8 km^3 was emplaced at depths of 0.2-0.4 km during the first month of the eruption in the transition from purely explosive to hybrid explosive-effusive activity (*Castro et al.*, 2016; *Delgado et al.*, 2019). The total erupted volume is ∼1.22 km^3 for the tephra erupted between June 4-7, 2011 (*Pistolesi et al.*, 2015) and ∼1.2 km^3 bulk (*Castro et al.*, 2016) to 1.45 km^3 DRE (*Delgado et al.*, 2019) for the lava flow and the shallow laccolith. Field observations in early January 2012 showed that the lava extrusion was coeval to a weak eruptive column, gas and ash jetting punctuated by short Vulcanian blasts (*Schipper et al.*, 2013). The erupted magma has a rhyolitic composition (explosive phase pumice 69.5% SiO_2, lava 71-72% SiO_2) that overlaps with the composition and rare earth elements of the 1960 and 1921-1922 eruptions, and was stored at depths between 2.5 and 6 km (*Castro et al.*, 2013; *Jay et al.*, 2014; *Wendt et al.*, 2017). The explosive phase magma was nearly aphyric resulting in a highly mobile rhyolite with fast ascent rates (*Castro et al.*, 2013).

4 InSAR methods

In this review I have included observations from almost every SAR mission available since 2003, which include ENVISAT, ALOS-1, TerraSAR-X/TanDEM-X (TSX/TDX), COSMO-SkyMED (CSK), RADARSAT-2 (RS2), UAVSAR, Sentinel-1 (S1) and ALOS-2 (Table 1). Data from ERS-1/2 are only briefly described due to its low quality (*Pritchard and Simons*, 2004). SAR data from the legacy JERS and RADARSAT-1 and from the newer SAOCOM-1 and PAZ missions are not available.

The first InSAR studies at Cordón Caulle (*Pritchard and Simons*, 2004; *Jay et al.*, 2014) used individual interferograms processed with a standard range-Doppler processing chain implemented in the legacy JPL ROI_PAC software (*Rosen et al.*, 2004). New algorithms and processing tools like SAR focusing with a motion compensated orbit (*Zebker et al.* 2010), geometric coregistration (*Sansosti et al.*, 2006) and zero-Doppler processing (*Eineder*, 2003) for individual interferograms and time series have been implemented in the JPL ISCE (*Rosen et al.*, 2012) and ISTerre/IPGP NSBAS (*Doin et al.*, 2011; *Grandin*, 2015) software. All the interferograms and time series presented in this study (Figure 3 - Figure 6) were processed with the ISCE software except two co-eruptive ENVISAT interferograms which were processed with the ROI_PAC software (Figure 4a-b, *Jay et al.*, 2014) and the Sentinel-1 descending time series (Figure 5) that was processed with the NSBAS software. Data processing is described in detail in the supplementary information (SI) and elsewhere (*Delgado et al.*, 2016, 2017). Due to the improvement of the InSAR workflows and a better data availability, I have used these new tools to reprocess interferograms from the now legacy ENVISAT and ALOS-1 missions presented in previous studies (*Jay et al.*, 2014; *Euillades et al.*, 2017; *Wendt et al.*, 2017). These results include new ALOS-1 time series and a source model for the first episode of ENVISAT-detected uplift between 2003 and 2007, which extend the sequence of pre-eruptive uplift from February 2007 (*Jay et al.*, 2014) to February 2003. Further, I have also expanded CSK, RS2 and S1 time series from May 2018 (*Delgado et al.*, 2018) to May 2020.

5 InSAR observations

In this section I describe all the deformation signals observed between 2003 and 2020 at Cordón Caulle.

5.1 Pre-eruptive ground deformation

5.1.1 1993-1996

Pritchard and Simons, 2004 presented a single ERS-1/2 interferogram that recorded 8 cm of subsidence at the Cordón Caulle graben during 1996-1999. The limited temporal resolution of this interferogram and the lack of other independent data results in a large degree of uncertainty in the interpretation of this deformation signal, which has been attributed to changes in the hydrothermal system of the volcano (Matthew Pritchard, personal communication). Therefore this data set is not considered further in this study.

5.1.2 2003-2007

The first unambiguous observations of ground uplift were recorded by ENVISAT IM2 ascending and descending interferograms (*Fournier et al.*, 2010) and span 2003 to 2007, with a maximum line-of-sight uplift rate of ∼3-4 cm/yr observed at the Cordón Caulle graben (Figure 3a-b and Figure S1). These interferograms can be modeled by the opening of a sub horizontal sill at a depth of 5.2 km with a total volume change of 0.013 km^3 during 2003-2007 (Supplementary Material).

5.1.3 2007-2011

A second pulse of uplift was detected by ALOS-1 ascending interferograms which recorded ∼30 cm during January 2007 and February 2008 (Figure 3c). The deformation signal is located on both Cordón Caulle and Cordillera Nevada caldera and can be modeled by two spherical sources at depths between 2.8 and 4.1 km, with a total volume change of 0.023 km^3 (*Fournier et al.*, 2010; *Jay et al.*, 2014). The poor temporal sampling of the data does not allow to properly assess the temporal evolution of uplift

A third pulse of uplift occurred during mid 2008 to early 2009, with a maximum uplift of ∼15 cm recorded by ALOS-1 ascending data. The deformation signal was observed in the W flank of Cordón Caulle and is different in location to that of the 2007-2008 episode (Figure 3). Because the line-of-sight (LOS) is the same than for the the 2007-2008 episode of uplift, the shift in location is produced by a different source compared to that of 2007-2008. Different deformation sources (small sphere, prolate spheroid, sill) can model the data, with depths between 5 and 9 km, although none can properly fit both ascending stacks and a single descending interferogram (Figure 3f). The source volume change during 2008-2009 is 0.03 km^3 for the spherical source (*Jay et al.*, 2014). *Jay et al.*, 2014 showed that uplift paused between 2009 and 2010, but the ALOS-1 time series shows that uplift continued from 2010 to 2011 (Figure 3). Therefore I consider that the episode lasted between May 2008 and January 2011.

Jay et al., 2014 observed a small uplift signal located within Cordillera Nevada caldera near the Trahuilco geyser (*Sepulveda et al.*, 2004) that occurred between February 13 2010 and March 31 2010 (Figure 3d). This deformation signal was modeled with a very shallow spherical source at a depth of 1.7 km with a volume change of 0.0014 km^3.

A fourth pulse of uplift with an amplitude of 5 cm was recorded by ENVISAT IM6 data during March-May 2012. The data can be modeled with a sill at a depth of 4 km with a total volume change of 0.003 km^3 (*Jay et al.*, 2014). However *Euillades et al.*, 2017 speculated that the signal observed in this interferogram could be an atmospheric artifact, but pair-wise logic could not be applied to discriminate between these two scenarios. Due to this discrepancy, this signal is not considered further.

Therefore, InSAR data suggests at least three pulses of pre-eruptive uplift at depths between 3 and 9 km. The simplest and most likely mechanism to explain these signals is magma injection in a shallow crystal mush underlying the volcano because the deformation sources are much deeper than the inferred depth of the shallow hydrothermal system (*Sepulveda et al.*, 2005, 2007; *Jay et al.*, 2014). The spatial shift in location of the deformation signals results from magma injection in different parts of the plumbing system of Cordón Caulle and will be discussed with detail later in the manuscript. The only exception is the localized deformation in the Trahuilco Geyser in early 2010, which *Jay et al.*, 2014 interpreted to be of hydrothermal origin in response to the dynamic triggering of the 2010 M_w 8.8 Maule earthquake.

5.2 Co-eruptive ground deformation

The co-eruptive ground deformation signals are different compared with those of the sequence of pre-eruptive uplift. The eruption started 2 months after the end of the ALOS-1 mission and during the ENVISAT extension mission. The latter was the only satellite that recorded data throughout the complete eruption and was the core data analyzed by all the studies that have studied the eruption with InSAR (*Jay et al.*, 2014; *Bignami et al.*, 2014; *Wendt et al.*, 2017; *Euillades et al.*, 2017; *Delgado et al.*, 2019), with five additional TSX and RS2 interferograms processed by *Delgado et al.*, 2019.

A 30-day interferogram that spans the first three days of the eruption (June 04-07 2011) shows 1.3 and 0.3 m of LOS subsidence at Cordillera Nevada caldera and Puyehue volcano respectively (Figure 4a, *Jay et al.*, 2014; *Bignami et al.*, 2014; *Wendt et al.*, 2017). The subsidence was produced by deflating sources located at depths of 3.8 and 6.1 km with a total volume change of $\sim$ 0.11 km^3 respectively. The deformation sources are offset 10-15 km from the eruptive vent which implies a mechanism of lateral magma transport from these lateral sources to the eruptive vent. Interferograms that span the rest of the eruption have no coherence on top of the volcano until the eruption waned and coherence increased during the 2011-2012 austral summer. Nevertheless, all of these data sets record several tens of centimeters of subsidence due to lava effusion (Figure 4b-c). The post June 7 2011 deformation signal can be modeled by a finite-sized prolate spheroid calculated with the finite element method based on the inversion for an analytic model (*Delgado et al.*, 2019), providing better model fits than previous attempts with a single Mogi source (*Jay et al.*, 2014; *Wendt et al.*, 2017). The spheroid depth is $\sim$5.2 km below the volcano, centered on the graben and oriented in the direction of the volcanic chain. The spheroid semi-major and semi-minor axes are 10 and 2.5 km respectively (Figure 4, Figure 7). *Delgado et al.*, 2019 inverted 20 coherent interferograms with the spheroid source fixed to retrieve a time series of pressure change that follows an exponential trend (shown in Figure 4 for the effusive phase only). The best-fit spheroid and the time series of pressure change predict a pressure drop of ∼20-50 MPa, a reservoir volume change of 0.5 km^3, and ∼2.2-2.7 m of LOS subsidence on top of the volcano (Figure 2). The data also suggests a slight change in the deformation source during the second half of the eruption, in agreement with a second pulse of lava effusion (*Bertin et al.*, 2015; *Coppola et al.*, 2017), but the change was minor and therefore not described here further. These three deflating sources (two during June 04-07 2011 and one during the rest of the eruption) are consistent with three bodies of magma tapped during the first week of the eruption (*Alloway et al.*, 2015). In general the depths of the spherical and prolate spheroidal sources of 4-6 km are in agreement with depths inferred from geobarometry (*Jay et al.*, 2014) and experimental decompression of the mineral phases observed in the erupted tephra (*Castro et al.*, 2013).

5.2.1 Lava flow effusion and laccolith intrusion

TanDEM-X CoSSC (Coregistered Slant range Single look Complex) data were acquired before and several times during the effusive phase of the eruption. These data were used to calculate six high-resolution DEMs that were subtracted to produce differential DEMs (dDEMs) that allow to calculate both time-averaged discharge rates (TADR) and time series of extruded volume. The dDEM data show a maximum thickness of ∼150 m for the lava flow and an area of topographic increase up to ∼250 m immediately east of the lava flow and the eruptive vent (Figure 4e-f). This area of uplift was interpreted and modeled by *Castro et al.*, 2016 to be produced by the intrusion of a laccolith at very shallow depths of ∼0.2-0.4 km below the surface. The time series of lava flow and laccolith intrusion volume shows an exponential trend with a total volume of ∼1.45 km^3 DRE during the whole eruption (Figure 2) and ∼1.2 km^3 DRE during the effusive phase of the eruption (Figure 4, *Delgado et al.*, 2019).

The temporal resolution of the TDX dDEM data (∼1 data point every 2 months) does not allow to pinpoint when did the laccolith intruded with respect to the explosive to effusive transition. Single Look Complex (SLC) amplitude images from ENVISAT and TerraSAR-X data were also used to track the growth of the laccolith (*Castro et al.*, 2016; *Delgado et al.*, 2019). Both studies conclude that the laccolith was emplaced during both the explosive and effusive phases of the eruption, starting probably during the first 4 days of the eruption and one week before the lava flow effusion. Pixel tracking calculated on these amplitudes images show range and azimuth displacements that exceed ∼20 m due to laccolith post-emplacement dynamics (Figure 4). The displacement is large enough that it can be observed directly in the coregistered amplitude images (not shown).

5.2.2 Physicochemical model of the effusive phase of the eruption

The 2011-2012 eruption is one of the few effusive eruptions to date where both time series of ground deformation and topographic change were acquired nearly simultaneously, and that showed quasi-exponential trends, like those observed in other eruptions (*Anderson and Segall*, 2011). This makes the 2011-2012 eruption one of the few of this kind where a time-dependent physicochemical model can be attempted, like at Mt St Helens (*Anderson and Segall*, 2013).

The physicochemical model developed by *Delgado et al.*, 2019 is adapted from *Anderson and Segall*, 2011, 2013 and simulates the pressure drop in a magma reservoir ($\Delta P(t)$) and the lava extrusion ($\Delta V(t)$) driven by this pressure drop. Here magma ascends to the surface through a conduit from a depressurized horizontal prolate spheroid reservoir that contains isothermal magma made up of melt, crystals, and exsolved and dissolved volatiles in a linear elastic half-space under a lithostatic load. As magma outflows from the reservoir, the flow rate is controlled by the conduit radius, reservoir pressure, and magma viscosity, which is a function of the dissolved H_2O and the crystal volume fraction. During the eruption, magma piles up on top of the eruptive vent, increasing the lithostatic load on the reservoir, and reducing the pressure gradient that drives the conduit flow. Since the data have no sensitivity to conduit processes, magma properties were assumed constant in the conduit and allowed to vary only in the reservoir, The model can be solved with different levels of complexities for constant magma properties (hereafter exponential model), constant magma properties but with a time-dependent surface load due to magma extrusion (hereafter lava load model) and time-dependent magma properties in the reservoir and with a time-dependent surface surface load (hereafter physicochemical model). The model parameters are the magma compressibility (β_m), conduit conductivity (ratio of the fourth power of conduit radius and magma viscosity) and pressure drop (p_{ch}) for the exponential and lava load models, and the initial overpressure, conduit radius, total CO_2 and H_2O in the magma for the physicochemical model. Equation 1 - Equation 2 show the analytic model (equations 1-4 in *Delgado et al.*, 2019 and A11-A12 in *Anderson and Segall*, 2011),

$$\Delta P(t) = -p_{ch}(1 - e^{-t/\tau}) \tag{1}$$

$$\Delta V(t) = V_0(\beta_m + \beta_{ch})p_{ch}(1 - e^{-t/\tau}) \tag{2}$$

with V_0 and β_{ch} the reservoir volume and compressibility and τ a time constant function of the plumbing system geometry. These models predict exponential-like trends for the reservoir pressure change and the extruded volume, like those observed in the data (Figure 4).

Despite the complexities of the eruption, the low coherence and the poor temporal temporal resolution of the InSAR data, *Delgado et al.*, 2019 found that the magma compressiblity of the lava flow and intruded laccolith during the effusive phase is $\sim 1 \times 10^{-10} Pa^{-1}$. This value is half that of the calculated compressibility for the erupted tephra of $\sim 2 \times 10^{-10} Pa^{-1}$ (*Jay et al.*, 2014). This is consistent with rhyolitic magma that was degassed with respect to its equilibrium condition at its storage depth of ∼5 km based on H_2O and CO_2 solubility models (*Delgado et al.*, 2019). The models also predict remarkably well the temporal evolution of the effusive phase, which follows an exponential trend for both the source pressure drop and extruded volume (Figure 4).

5.3 Post-eruptive inflation

A significant technological change occurred during the end of the eruption. The end of the ENVISAT extension mission coincided with the onset of CSK acquisitions which resulted in an increase in the data temporal resolution by more than one order of magnitude. This resulted in the application of dense InSAR time series for the first time in the volcano with CSK and RS2 stripmap data (*Delgado et al.*, 2016; *Euillades et al.*, 2017).

Deformation following the eruption started almost immediately, with uplift at an extremely fast rate up to 45 cm/yr during March 2012 - January 2013 – the fastest ever detected with satellite geodesy (GPS, InSAR) at a rhyolitic volcano. The uplift rate decreased in March 2013 to ∼17 cm/yr until May 2015 when deformation abruptly ended. The uplift can be modeled by a pressurized subhorizontal distributed opening sill at a depth of 6.2 km with a volume change of 0.125 km^3 (*Delgado et al.*, 2016, uniform opening sill shown in Figure 5). The time series of uplift during 2012-2015 follows an exponential trend which was interpreted by *Delgado et al.*, 2016 to be evidence of magma injection (e.g., *Lengline et al.*, 2008; *Le Mével et al.*, 2016), although at the time other deformation mechanisms could not be ruled out. *Delgado et al.*, 2018 tested whether the exponential trend could result due to viscoelastic relaxation following a transient pressure increase in the magma reservoir. They concluded that a model of a pressurized spheroid surrounded by a Maxwell viscoelastic shell with a viscosity of 2×10^{17} Pa s and a 1 km radius and with a transient pressure function of the form $P = P_f(1 - e^{-t/\tau})$ with τ=0.4 years, P_f=10 MPa could fit the data. However, the fit was worst than the magma injection model in an elastic medium, ruling out viscoelastic effects.

After one year with no deformation, uplift resumed in July 2016 until February 2017 (*Euillades et al.*, 2017; *Delgado et al.*, 2018). This episode of uplift marks the first time that a complete multiparametric set of X, C and L band observations from ascending and descending CSK stripmap, S1 TOPS, RS2 Wide Ultra Fine and Wide Fine stripmap and ALOS-2 ScanSAR and stripmap data image the same episode of ground deformation at the volcano. The uplift event reached ∼12 cm in 6 months – equivalent to an uplift rate of ∼24 cm/yr, and ended abruptly in February 2017 as it did during May 2015. The spatial footprint of the deformation signal is very similar to that of the 2012-2015 episode of uplift. *Delgado et al.*, 2018 tested whether the uplift was due to a different source and concluded that it is the same deformation source active during 2012-2015, but with a much smaller volume change of ∼0.022 km^3. This yields a total source volume change of 0.147 km^3 during March 2012 - February 2017. The lack of interferometric coherence during the winter with C and X-band data and the poor temporal sampling of ALOS-2 L-band data did not allow to assess whether the time series of the 2016-2017 episode of uplift follows an exponential or a double exponential trend as observed elsewhere (*Le Mével et al.*, 2016).

Delgado et al., 2018 showed potential evidence for a third pulse of uplift during May 2017 - May 2018, but the limited amount of data did not allow to confirm this. New GPS and InSAR observations from CSK, RS2 and S1 (Figure 5) show that deformation continued beyond May 2018 during a third episode between May 2017 - May 2019, with a rate of ∼5-6 cm/yr depending on the data set and resulting in a total of 1 m of post-eruptive uplift. As during 2016-2017, the deformation signal during 2017-2019 is very similar to that of 2012-2015 suggesting the same deformation source (Figure 5).

5.3.1 Lava flow and laccolith post-emplacement ground deformation

Delgado et al., 2016 presented small baseline RS2 and CSK interferograms spaning two weeks during 2013 and 2014 that recorded ∼5-6 cm of LOS subsidence in the lava flow, resulting in rates of ∼1.2-1.4 m/yr. However, the lack of a high resolution DEM at the time of that study did not allow to better track the flow subsidence, reducing the analysis to individual interferograms. A small-baseline stack of RS2 Wide Ultra Fine interferograms that spans February to May 2016 plus two ALOS-2 SM3 interferograms during 2015-2016 show a complex pattern of lava flow subsidence with rates up to 0.5 m/yr in some areas of the flow. Other areas of the flow show either uplift or eastward movement towards the satellite. These signals cannot be attributed to a simple mechanism of homogeneous lava flow cooling and subsidence (e.g., *Ebmeier et al.*, 2012) and imply that sections of the flow were mobile, probably flowing laterally four years after the end of the eruption. The extreme thickness of the lava flow suggest that subsidence produced by cooling can last for several decades (e.g., *Chaussard*, 2016). The RS2 stack shows subsidence in the E part of the laccolith, although analysis of 2016 TanDEM-X bistatic interferograms shows that the phase in the laccolith is proportional to the perpendicular baseline, suggesting a DEM error in that area (Figure 6, SI).

6 Discussion

Here I discuss some interesting observations and lessons learned from the Cordón Caulle InSAR data and models. These include mainly the long term evolution of the plumbing system of the volcano, the triggering mechanism and the temporal evolution of the 2011-2012 eruption.

6.1 Deformation sources

Source modeling approaches for Cordón Caulle have ranged from the use of simple spherical models (*Jay et al.*, 2014) to viscoelastic finite element models (*Delgado et al.*, 2018) and physicochemical models that couple the reservoir pressure drop, conduit flow and magma physicochemical properties (*Delgado et al.*, 2019). Despite their simplicity, in general analytic and numerical source models explain the InSAR ascending and descending data well. However, *Jay et al.*, 2014 could not fit the ascending and descending ALOS-1 data for the 2008-2011 uplift pulse with an analytic model, which suggests that a more complex source geometry is required to model that specific pulse of pre-eruptive uplift.

In general deformation sources are scattered along the extent of the volcanic chain, but clustered near Cordón Caulle (Figure 7). The similarity of the deformation sources during 2003-2007, 2007-2008, 2011-2012 during the effusive phase, and 2012-2017 suggest a common zone of magma storage and effusion, which could occur as a neutral buoyancy level at depths of 4-6 km (Figure 7). This is in agreement with numerical models that show that magma is preferably stored at those depths (*Huber et al.*, 2019). Further, this deformation zone has been episodically active before and after the eruption with slight changes in the source geometry. For example, the model for 2012-2017 cannot fit well the 2007-2008 data (not shown). This source stability in location and time and episodic unrest is similar to other basaltic reservoirs like Okmok (*Lu et al.*, 2010; *Lu and Dzurisin*, 2010, 2014) and Kilauea (*Poland et al.*, 2014). In general source spatial migration and stability are not well understood but could be due just to discrete pulses of magma injection occurring across the volcano (e.g.,*Dzurisin et al.*, 2012). The reason why the 2012-2019 sill source is more stable in location compared with the pre-eruptive sources is unknown. All these observations suggest a large shallow plumbing system (*Jay et al.*, 2014; *Delgado et al.*, 2016) made up of either one large crystal mush or several individual reservoirs under cold storage conditions (*Cooper and Kent*, 2014) into which magma is episodically stored and injected. These observations also suggest that the plumbing system of Cordillera Nevada and Puyehue are connected to that of Cordón Caulle, despite the three volcanoes having evolved independently (*Singer et al.*, 2008). To what extent the magmas of the three volcanoes interact mechanically, chemically or thermally with each other is currently unknown.

The InSAR data indicates that pressure sources instead of dikes can model the data during the onset of the eruption. This hypothesis was explored by *Wendt et al.*, 2017 and the transition between the explosive and effusive stages of the eruption is better explained with a dike opening model than pressure sources (*Castro et al.*, 2013). *Wendt et al.*, 2017 calculated models of a dike and a sphere for the interferogram that spans the first three days of the eruption (Figure 4a), but the model fit was significantly worst than a two sphere model. During the rest of the eruption the prolate spheroid models of *Delgado et al.*, 2019 can fit the data very well with no need to invoke a dike. Although the dike intrusion is a very plausible idea, the extent of phase decorrelation observed during the onset of the eruption implies that the existing InSAR cannot unambiguously address this point. Very high resolution pixel tracking on TSX stripmap data have the potential to unravel the role of co-eruptive diking.

Despite the good fit of the models to the InSAR data, these models are oversimplfications of magmatic systems. Magma reservoirs are crystal mushes (*Bachmann and Bergantz*, 2008) which are better understood in terms of poroelastic mechanisms, but at the day of now these models are novel (e.g., *Liao et al.*, 2018) and have not been used to model ground deformation data. Further, these models have a lot of parameters that trade-off with each other and that are not straightforward to constrain with geodetic data. Future studies should consider reservoirs with more arbitrary geometries like the compound dislocation model *Nikkhoo et al.*, 2016, spheroids of finite-sized dimensions (*Le Mével et al.*, 2016; *Delgado et al.*, 2019) and poroelastic models (e.g., *Liao et al.*, 2018). Also, the similar location and shape of the deformation sources (Figure 7, *Euillades et al.*, 2017) suggests that future studies may also attempt a model that explains jointly the pre-eruptive, co-eruptive and post-eruptive ground deformation data with a common source (e.g., *Lu and Dzurisin*, 2010).

6.2 Eruption triggers

Forecasting eruptions is one of the key questions in volcano science (*Sparks et al.*, 2012) and the InSAR observations at Cordón Caulle make this a promising case from which we can draw insights that may improve forecasting of other eruptions. Any triggering mechanism for the 2011-2012 eruption must account for the following facts: a) the eruption was preceded by a transient sequence of at least three pulses of pre-eruptive uplift lasting between 6 months and 4 years or more. (Figure 2, Figure 3), b) deformation sources that are scattered along the volcanic chain (Figure 1), c) rhyolites are stored as crystal mushes under cold storage conditions and are thermomechanically remobilized by magma injection that enhances melt percolation towards the liquid-rich cap on top of the mush (*Huber et al.*, 2010, 2011), and d) ground uplift of very low magnitude to none (Figure 3) and an increase in the seismicity between February and April 2011 (*Wendt et al.*, 2017). Despite the variety of processes that can be observed and modeled in crystal mushes (*Bachmann and Bergantz*, 2006; *Huber* *et al.*, 2012; *Papale et al.*, 2017; *Morgado et al.*, 2019), including segregation and merging of melt-rich layers within a transcrustal mush (*Sparks and Cashman* 2017), at the day of now all models of ground deformation in volcanoes fall under either of two generic categories: magmatic or hydrothermal processes. The former includes basalt injection that pressurizes the plumbing system, magma mixing, thermal heating without mixing and volatile exsolution among others. For example, it is possible that basalt was injected below Cordón Caulle and did not mix with the crystal mush, only providing the heat to melt a fraction of the mush (e.g., *Morgado et al.*, 2019). Nevertheless, the vast majority of the InSAR studies argue for injection of molten basalt that pressurizes the reservoir walls without further detail. Since eruptions are triggered by magma injection on time scales shorter than a decade (e.g., *Degruyter and Huber*, 2014; *Townsend and Huber*, 2020), in the following I will only consider the reservoir pressurization and rupture produced by magma injection.

A general rupture criteria (*Tait et al.*, 1989; *Pinel and Jaupart*, 2003; *Albino et al.*, 2010) shows that a dike can propagate from the chamber to the Earth's surface once the deviatoric component of the minimum compressive stress in the reservoir walls is greater or equal than the tensile strength of the rock. This means that the magma overpressure is twice the tensile strength of the rock for a spherical reservoir in an infinite medium (*Tait et al.*, 1989; *Albino et al.*, 2010). An extension of the previous criteria that considers both magma overpressure and buoyancy for pressurized cavities in an elastic medium is (*Sigmundsson et al.*, 2020)

$$\Delta\rho g h + \Delta P_{magma} \geq \sigma_{failure} + \sigma_{external} \tag{3}$$

with the terms from left to right the buoyancy force due to a magma body of thickness h, and density contrast $\Delta\rho$ under gravity acceleration g, the magma overpressure ΔP_{magma}, $\sigma_{failure}$ the failure limit and $\sigma_{external}$ stress due to other processes (surface loading, flank instability, transient changes in tectonics stresses, etc). In the absence of external triggers ($\sigma_{failure} = 0$), an eruption can be triggered by an increase in the magma pressure due to compressible or incompressible magma injection (ΔP_{magma}), an increase in the thickness of a buoyant magma body or an increase in the density of the buoyant magma body due to magma phase transitions in the reservoir, or all of the previous.

The 2003 to 2011 deformation sources are at depths of 4 to 9 km, which suggests that episodic magma injection with a time-variable rate in a large elongated reservoir at a level of neutral buoyancy is potentially responsible for triggering the eruption. Under the assumption that the deformation is due to magma injection, the volume change of 0.013 km^3 during 2003-2007 plus the 0.05 km^3 during 2007 and early 2011 results in the intrusion ~0.063 km^3 of incompressible magma. This volume is one order of magnitude lower than the volume of erupted magma and the co-eruptive source volume change, even accounting for magma compressibility. The 2003-2007 source volume change is much smaller than the source volume changes during 2007-2011 (*Jay et al.*, 2014) therefore their role on potentially triggering the eruption are very minor. The previous argument suggests that if the eruption was triggered by magma injection until the reservoir walls ruptured when the hoop stress reached the tensile strength of the rock, a significant amount of magma must have been intruded before 2003 (*Jay et al.*, 2014). Unfortunately the volume of this potential magma is unconstrained due to the lack of geodetic data before 1996. Therefore, other mechanism like volatile exsolution (*Tait et al.*, 1989) since the previous eruption in 1960 eruption cannot be ruled out. It is also possible that reservoir was brought closer to failure due to magma buoyancy without significant reservoir pressurization that can be detected geodetically (e..g, *Sigmundsson et al.*, 2020). An alternative mechanism is that magma injection in different parts of the plumbing system of the volcano increased the failure pressure by lateral stress transfer (*Albino and Sigmundsson*, 2014). In this mechanism magma injection in a specific section of the plumbing system can increase the failure pressure in other regions below the volcano, without the need for mass injection in the reservoir from which magma will eventually erupt. This mechanism is conceptually equivalent to earthquake triggering by an increase in the static Coulomb stress. The normal stress σ_{rr} in a spherical source embedded in a full space is given by

$$\sigma_{rr} = -\frac{\Delta V G}{2\pi r^3} \tag{4}$$

with ΔV the source volume change, G the shear modulus and r the distance (equations 7.7 and 7.13 in *Segall*, 2010). The negative sign indicates compression, so a positive volume change produces compression. A volume change of 0.03 km^3 in the 2008-2011 source with G=20-2.1 GPa (*Delgado et al.*, 2019; *Heap et al.*, 2020) can increase the radial stress to 0.06 - 2 MPa over distances of 5-7 km, similar to the distance between the 2007-2008 and the early June 2011 deformation sources (Figure 8). If either of these reservoirs were in a critical state, these stresses due to magma injection can influence the reservoirs and potentially bring them closer to failure (e.g., *Albino and Sigmundsson*, 2014; *Biggs et al.*, 2016).

In summary the InSAR observations allow for multiple mechanisms to explain the eruption triggering. It is also likely that several of these triggering mechanism were coeval and that InSAR just recorded a very low resolution image of these processes (e.g., *Bachmann and Huber*, 2016; *Lowenstern et al.*, 2017). Further, the time span covered by the pre-eruptive InSAR observations of ground uplift is only 8 years and it is so short with respect to the previous eruption in 1960 and the time scales of magmatic processes so it is very difficult to disentangle the relevant contribution of these individual processes. Thereby, the complete lack of ground instrumental data before 2010 when seismic monitoring started and the total lack of other observations before 1996 do not allow to unambiguously unravel the triggering mechanism. Due to the large deformation in the past two decades, pixel tracking from either historical satellite or airborne imagery could provide insights on these processes (e.g., *Derrien et al.*, 2015).

6.3 Eruption temporal evolution

Despite the complexity of the eruption with two pulses of lava effusion (*Coppola et al.*, 2017), the intrusion of a shallow laccolith (Figure 4), and three sources of ground deformation (Figure 7), both the erupted volume and pressure change time series derived from InSAR can be explained reasonably well with a simple model. The model is made of a finite-sized spheroid that deflates in response to lava effusion through a conduit, with both the effusion and the deflation following exponential trends (Equation 1-Equation 2). It is true that deviations from exponential trends (e.g., *Kubanek et al.*, 2017) require more complex models including magma permeability (e.g., *Wong and Segall*, 2019) or a widening dike/conduit (e.g, *Castruccio et al.*, 2017), but the simple trends observed in the data during the effusive phase do not require such level of complexity. The key finding of the physicochemical models is that the magma compressibility during the effusive phase is significantly lower compared with the compressibility inferred for the magma erupted during the explosive phase. This is a consequence of a partially degassed rhyolite with respect to the predicted dissolved H_2O and CO_2 for a storage depth of ∼5 km (*Delgado et al.*, 2019). On the other hand, a relevant question is why did the deflating sources shift from Cordillera Nevada caldera and Puyehue volcano to the Cordon Caulle graben during the first month of the eruption? (Figure 4a-b). Since magma flow is proportional to the pressure gradient, the first two reservoirs had less magma capable of flowing than the third one or their hydraulic conductivity decreased very rapidly compared with that of the source below Cordon Caulle. This is a topic that requires further studies.

6.4 Mechanisms of unrest during pre and post-eruptive uplift

The similarities in the ground deformation during the transient uplift in 2003-2007, 2007-2008 and 2012-2019 and their chronology with respect to the eruption suggest that the same processes are responsible for observed signals, which for simplicity I related to magma injection. Since the 2012-2015 uplift started immediately after the end of the eruption, this episode of unrest can be easily explained as a pulse of magma injection. This episode was triggered by the 20-50 MPa co-eruptive pressure drop (*Delgado et al.*, 2019), allowing magma to flow from a deep mantle source to the shallow sill source (e.g., *Lengline et al.*, 2008; *Delgado et al.*, 2016). The prediction of this mechanism is a decreasing exponential trend in the ground deformation data which was observed during 2012-2015 (Figure 5, *Delgado et al.*, 2016; *Euillades et al.*, 2017). The similarity in the deformation pattern between the 2012-2015, 2016-2017 and 2017-2019 pulses of uplift suggest that the three are produced by magma injection in the same reservoir, although the time series does not show evidences of exponential signals (Figure 4). On the other hand, viscoelastic relaxation produced by transient pressurization followed by stress relaxation in a viscous shell surrounding the reservoir was found to be not important during 2012 and 2015 (*Delgado et al.*, 2016). This does not rule out that more complex viscoelastic rheologies (e.g., *Head et al.*, 2019) or a more realistic pressure functions can explain the data equally well than the magma injection model. Also, this does not rule out that viscoelastic relaxation is important over longer time scales (10-100 years).

It is also striking that some of these episodes of uplift can be very short, ranging from ~6 months to several years. However, their episodic nature for both the onset and end of uplift is not predicted by the models of pressure-driven magma injection because they assume that injection is a prescribed boundary condition. The only option is to incorporate some aspect of the internal dynamics of magma reservoirs into these models (*Walwer et al.*, 2019). *Delgado et al.*, 2016 cited inelastic effects such as conduit clogging to explain the abrupt end of the deformation in 2015, as it occurred before the exponential trend in the data reached a value close to its asymptote (Figure 5). The factors controlling the transient deformation before the eruption are also relevant. However, the poor temporal resolution of the 2003-2011 data does not allow to resolve the actual onset and end of the episodes of uplift within several months or even years (Figure 3).

Rhyolitic genesis at Cordón Caulle suggests fractional crystallization from basaltic melts (*Gerlach et al.*, 1988; *Singer et al.*, 2008), raising the questions to whether the InSAR data are sensitive to the composition of the magma injected in the storage level of neutral buoyancy or not. *Delgado et al.* 2018 used the Poiseuille flow law (*Jaupart*, 2000) to infer the magma composition and concluded that the problem is ill-conditioned because the magma viscosity – a proxy for composition, depends on the fourth power of the conduit radius. This parameter is poorly constrained and this uncertainty results in a wide range of magma viscosities spanning many orders of magnitude. Studies on basaltic systems estimate conduit radii of 1-5 m (*Fukushima et al.*, 2010; *Pedersen and Sigmundsson*, 2006) and these values indicate that the injected magma at Cordón Caulle must be basaltic. Therefore, at the moment InSAR cannot provide robust constrains on the magma composition during transient episodes of uplift.

I infer that successive intrusions in the remarkably stable level of neutral buoyancy at ~6 km depth result in the coalescence of these magma bodies on time scales of 10-100 kyr, while the individual magma injections during 2003-2019 should not be able to coalesce on these short scales of less than 10 years (*Biggs and Annen*, 2019). Therefore, these multiple injections rejuvenate the system thermally but do not interact chemically with each other (e.g., *Morgado et al.*, 2019). Instead, these individual and small pockets of melt might remain molten and isolated as high melt fraction magma surrounded by the much bigger crystal mush (e.g., *Gansecki et al.*, 2019). Finally, is it possible that the InSAR data shows evidence of a mush reorganization process that occurs at depths between 4 and 8 km due to volatile exsolution? Here layers of melt can segregate and migrate over multiple levels in the upper crust (*Cashman et al.*, 2017; *Sparks and Cashman*, 2017; *Sparks et al.*, 2019). I consider this a plausible situation for the storage depths of 4-9 km and deserves its detailed analysis. Geophysical imaging like seismic tomography should be able to provide insights between these scenarios.

Despite the 1 m of post-eruptive uplift between March 2012 until April 2019, the likely injection of magma has not resulted in an eruption. The injection of 0.146 km^3 (*Delgado et al.*, 2018) of magma, most likely basalt, is significantly smaller than the co-eruptive volume change of $\sim$0.6 km^3 (*Jay et al.*, 2014; *Delgado et al.*, 2019) and about twice the volume change of the pre-eruptive sources during 2003-2011. I use the rupture criteria of *Browning et al.*, 2015 to estimate the maximum rupture pressure p_e for an individual episode of magma injection (Equation 5 - Equation 6).

$$p_e = \frac{\Delta V_m}{V_m \beta} \tag{5}$$

$$V_m = \frac{V_e}{T_0 \beta} \tag{6}$$

Here V_m is the volume of the reservoir, V_e is the erupted volume, T_0 is the tensile strength of the rock, β is the combined reservoir and magma compressibility, p_e is the reservoir overpressure and ΔV_m is the volume of the injected magma. Assuming an erupted volume $V_e = 2.2$ km^3 that includes the tephra (1 km^3), the lava flow and the shallow laccolith (1.2 km^3 DRE, *Delgado et al.*, 2019) and an intruded volume $\Delta V_m = 0.145$ km^3 during March 2012 and February 2017 and a tensile strength of the rock $T_0 = 20$ MPa, then the maximum pressurization in the reservoir is $p_e = 1.3$ MPa. Therefore, I hypothesize that it will take several decades to reach the same failure threshold inferred before the 2011 eruption and with pulses of episodic injection similar to those observed during 2012-2019. This assumption only holds if the mechanical conditions on the reservoir are time-invariant which is rarely the case (e.g., *Carrier et al.*, 2015).

6.5 Structural control of an active magma intrusion

Cordón Caulle is considered a landmark case of a volcano in the SVZ where the local structural setting plays a role controlling magma and eruption dynamics (*Lara et al.*, 2004, 2006a,b; *Cembrano and Lara*, 2009; *Wendt et al.*, 2017). By tectonic control I refer to the structural heritage and not to the current neotectonic characteristics of the SVZ. The volcanic chain is emplaced on top of a NW-SE regional basement structure that is misoriented with respect to the current kinematic regime of the SVZ and could be resheared to favor magma emplacement by static stress changes triggered by a megathrust earthquake (e.g., *Lara et al.*, 2006b; *Cembrano and Lara*, 2009). All the vents of the 1921-1922, 1960 and 2011-2012 eruptions are located on both the footwall and hanging wall of the inferred normal faults that bound the Cordón Caulle graben, but I have not observed in the InSAR data conclusive evidence for triggered fault slip on any of these structures. *Delgado et al.*, 2016, 2018, 2019 suggested that as co- and post-eruptive deformation sources are elongated in the direction of the local volcanic chain they are tectonically controlled as proposed for the long-term evolution of the volcano (Figure 4-Figure 5). Indeed, all the deformation sources except for the 2008-2011 pulse are elongated in the direction of the volcanic chain (Figure 7). It is possible that the local structure that produces the NW-SE alignment of Cordón Caulle is a source trap that enhances magma storage at the level of neutral buoyancy of ~4-9 km, resulting in deformation signals aligned in this direction and rotating the local stress tensor (e.g., *Lara et al.*, 2006b). *Wendt et al.*, 2017 explored the idea that the deformation during the first three days of the eruption was produced by a tectonically controlled dike (*Castro et al.*, 2016), but none of their dike models provide a significant better fit than two deflating spherical sources. Therefore the role of the local tectonics driving the emplacement of magma into the upper crust and their interaction with local faults (e.g., *Lundgren et al.*, 2017; *MacQueen et al.*, 2020) is yet to be explored more thoroughly. The absence of triggered fault slip is similar to Laguna del Maule (LdM) where none of the InSAR studies have found any conclusive evidence for triggered fault slip despite the ~ 2.1 m of uplift between 2007 and 2016 (*Feigl et al.*, 2014; *Novoa et al.*, 2019; *Zhan et al.*, 2019). Very long InSAR time series (≥ 10 years) might resolve such small fault slip signals in the future.

6.6 Lava flow rheology

The key finding of the InSAR dDEMs is that rhyolitic lava flows are counter-intuitively very mobile, in agreement with other observations (*Tuffen et al.*, 2013; *Magnall et al.*, 2017). The extreme thickness of the lava flow could not be properly inferred from field observations (*Bertin et al.*, 2015), which recorded a thickness 4 times smaller compared to that of the dDEM data (*Castro et al.* 2016; *Delgado et al.* 2019). This shows that the planimetric approach that assumes a constant thickness to calculate the lava flow volume does not provide reliable results (e.g., *Pedersen et al.*, 2018). The TADR during most of the eruption varied between 10 and 150 m^3/s (*Castro et al.*, 2016; *Delgado et al.*, 2019) and is much larger than the TADR of much smaller basaltic and dacitic eruptions, which tend to average 0.5 - 10 m^3/s (*Poland*, 2014). The high TADR from the extrusion of a very large volume of lava is similar to that of other large basaltic eruptions studied with InSAR-derived dDEMs, including the 2018 Kilauea eruption with ~70 DRE m^3/s (*Lundgren et al.*, 2019) and the 2012-2013 Tolbachik eruption with ~ 100-400 m^3/s (*Kubanek et al.*, 2017). This implies that the rhyolite viscosity during the effusive phase was as low as it can be according to theoretical models (*Castro et al.*, 2013) or the conduit radius was very wide. On the other hand, the lava flow subsidence rate of ~1.2-1.4 m/yr is quite fast compared with other subsiding lava fields (*Ebmeier et al.*, 2012; *Carrara et al.*, 2019) and four years after the end of the eruption the lava flow displayed a complex pattern of subsidence and motion in the range direction (Figure 6). Future studies should consider the rhyolite rheology (*Fink*, 1980) to better explain these observations as well as other data (*Tuffen et al.*, 2013; *Farquharson et al.*, 2015; *Magnall et al.*, 2017).

6.7 Coupling between the magmatic and hydrothermal system

Cordón Caulle hosts the largest hydrothermal system of the SVZ (*Sepulveda et al.* 2004, 2007), with five fumarolic fields (Figure 1) which are likely to be coupled to the magmatic system of the volcano. The role of the hydrothermal system to produce ground deformation has been considered to be negligible with respect to the magmatic system because the InSAR-derived sources of deformation are much deeper than those inferred for the hydrothermal system (*Jay et al.* 2014). The only exception is the uplift recorded near the Trahuilco geyser inside Cordillera Nevada (Figure 1). This area deformed right after the 2010 Maule earthquake (Figure 3d) and the source model is 2-3 times shallower than the rest of the deformation sources, ruling out a magmatic origin. The spatial coincidence between deformation, the dynamic triggering by the earthquake and an hydrothermal system suggest that the passage of seismic waves produced transient changes in permeability that can induce groundwater flow resulting in ground deformation (e.g., *Manga et al.* 2012; *Pritchard et al.* 2013).

The large amount of hydrothermal vents in the volcano suggests that the previous argument to neglect the role of the hydrothermal system on modulating the episodes of unrest is too simplistic. For example, *Chang et al.*, 2007 have shown that magma injection in sills can induce the flow of magmatic brines between multiple sources of deformation below Yellowstone caldera. Also, pressurization in hydrothermal systems can produce ground deformation signals that resemble those of magmatic origin (e.g., *Hurwitz et al.*, 2007). *Pritchard et al.*, 2019 have shown that time-lapse gas monitoring and microgravity measurements can reduce the ambiguity on the driving mechanisms of ground deformation but unfortunately neither have ever been attempted at Cordón Caulle. Further, at the time of writing no detailed analysis have been carried out on the volcano hydrothermal vents after the 2011-2012 eruption. Future studies should consider to what extent the hydrothermal and the magmatic system are coupled.

6.8 Comparison with other systems

6.8.1 Eruption triggering

The triggering mechanism of the 2011-2012 eruption is a matter of debate as described earlier. Similar situations were observed at Eyjafjallajökull, Grímsvotn and Okmok volcanoes that have repeatedly displayed ground deformation before several eruptions despite the differences in magma composition and tectonic setting between the SVZ, the North Atlantic rift and Aleutians subduction zone. At Eyjafjallajökull, InSAR detected transient pulses of uplift interpreted as magma intrusion that occurred more than 10 years and a few months before its 2010 eruption (*Pedersen and Sigmundsson*, 2006; *Hooper*, 2008; *Sigmundsson et al.*, 2010), with a potential eruption triggering due to lateral stress change (*Albino and Sigmundsson*, 2014). At Grímsvotn, GPS data have recorded two cycles of pre-eruptive uplift with exponential trends indicative of magma injection leading to two eruptions (*Reverso et al.*, 2014; *Bato et al.*, 2018; *Sigmundsson et al.*, 2018). At Okmok, InSAR has also recorded cycles of co-eruptive subsidence and pre and post-eruptive uplift that follow exponential trends indicative of magma injection and extrusion (*Lu et al.*, 2010; *Lu and Dzurisin*, 2010, 2014; *Biggs et al.*, 2010). These examples suggest that to some extent the geodetic signals that can be observed on yearly to decadal time scales during cycles of magmatic unrest and eruption are independent of the tectonic setting and of the chemical composition of the erupted magma.

6.8.2 Eruption dynamics

The InSAR observations of co-eruptive deformation are difficult to compare with other similar events due to the lack of other rhyolitic eruptions with instrumental observations. The 2008-2009 dome-forming eruption of Chaiteén volcano is the only one of these events and was triggered by a dike intrusion (*Fournier et al.*, 2010; *Wicks et al.*, 2011), resulting in a very asymmetric different deformation signal compared to that of Cordón Caulle. In terms of its temporal evolution, ground deformation was negligible during more than half of the eruption (*Pina-Gauthier et al.*, 2013; *Reath et al.*, 2019) and the dome extrusion followed an exponential trend for the first three months while during the rest of the eruption there is no constraining data (*Pallister et al.*, 2013). Therefore it is not clear how representative are the deformation signals of the 2011-2012 eruption of other rhyolitic eruptions. In terms of the co-eruptive ground deformation and extruded volume, similar exponential signals were recorded at Mt St. Helens (*Anderson and Segall*, 2013) and Sinabung (*Hotta et al.*, 2017; *Nakada et al.*, 2017) volcanoes for both types of data.

6.8.3 Transient uplift

In general deformation rates larger than 20 cm/yr are rare in subduction zone volcanoes (e.g., *Fournier et al.*, 2010; *Henderson and Pritchard*, 2013) and Cordón Caulle has had these rates at least three times. The only equivalent system is Laguna del Maule (*Feigl et al.*, 2014; *Le Mével et al.*, 2015) with a maximum of 28 cm/yr, which is still ∼50% less than the maximum of 45 cm/yr recorded in 2012. Other rhyolitic volcanoes like Yellowstone (*Chang et al.*, 2007; *Dzurisin et al.*, 2012; *Tizzani et al.*, 2015) and Long Valley (*Montgomery-Brown et al.*, 2015) have much lower satellite-detected deformation rates of 1-10 cm/yr. Compared with other rhyolitic systems, transient changes in the ground deformation that occur on time scales of ∼0.5-1 years are much faster at Cordón Caulle than at the aforementioned, so fast that they are akin to those observed at basaltic calderas (e.g., *Poland et al.*, 2012). Changes in the uplift rate at Yellowstone (*Dzurisin et al.*, 2012) and Laguna del Maule (*Le Mével et al.*, 2015) have been related to seismic swarms, but they have never been observed at Cordón Caulle (*Delgado et al.*, 2018). Therefore, Cordón Caulle can be considered a quite anomalously fast deforming volcano for both the uplift velocity and the transition from quiescence to unrest and back to quiescence.

6.9 An integrated view from InSAR, petrology and field observations

Figure 9 summarizes my geological interpretation on the plumbing system of Cordón Caulle for the time period between March 2003 and May 2020. The volcano is underlain by a laterally extensive plumbing system that extends from Cordillera Nevada caldera to Puyehue volcano, which is a crystal mush with melt-rich pockets that segregate to the liquid-rich cap on top of the mush through compaction and other mechanisms (e.g., *Bachmann and Bergantz*, 2006). In the absence of data other than InSAR, I suggest that ground uplift results from basalt injection into the crystal mush, potentially triggering melt extraction, although the exact details cannot be inferred with the existing data. Magma injections likely occurred during 2003-2007, 2007-2008, 2008-2011 and scattered across the volcanic chain. During the onset of the eruption, two reservoirs located below Cordillera Nevada caldera and Puyehue volcano deflated during the first three eruption days. During the rest of the eruption, a single reservoir deflated, and coeval with lava effusion and a shallow laccolith intrusion. These three reservoirs drained distinct areas of the plumbing system of the volcano. Afterwards, three pulses of likely magma injection were intruded in the same area from where magma was intruded before the eruption and drained during the effusive phase of the eruption. In general, all the deformation sources lie at depths between 4 and 9 km, with no InSAR nor petrological evidence for deeper sources (*Castro et al.*, 2013; *Jay et al.*, 2014). Hence, unrest does not occur at multiple levels throughout the crust and I consider this volcano to be a translateral instead of a transcrustal magmatic system (*Cashman et al.*, 2017; *Sparks et al.*, 2019), with likely stress interactions between the sources. By translateral I imply that unrest occurs in multiply places along the laterally extensive shallow plumbing system.

7 InSAR technological challenges

Although the InSAR data availability at Cordón Caulle has increased exponentially in the past decade, significant technical challenges remain in this area for a wider use of InSAR. These challenges are the limited and non-ideal data coverage and systematic coherence loss.

7.1 Data availability

During most of 2003-2012, descending SAR images that would result in coherent interferograms were seldom available and only since May 2013 CSK brought ascending and descending acquisitions to the same temporal resolution. Data from the current TSX, CSK, RS2, S1 and ALOS-2 missions have been acquired with different degrees of temporal resolution at the volcano. TSX data were only systematically acquired during the onset of the eruption, but not during the end and during the post-eruptive uplift. CSK data are the most consistently acquired data to date in the volcano, with a time series that spans between March 2012 and August 2020. RS2 data have been acquired with four different stripmap beams during the eruption and the sequence of post-eruptive uplift. This has allowed to compare the quality of these modes and beams (*Pritchard et al.*, 2018), but at the same time has hampered the systematic acquisition of a long time series. S1 data were acquired every 24 days between October 2014 until February 2017 when the mission started to acquire data every 12 days in the descending track. However ascending acquisitions were then stopped until November 2018 when they were restarted every 6 days after a special request to the European Space Agency. Afterwards they were reduced to every 12 days in June 2019. ALOS-2 acquired ScanSAR data every 42 days since burst synchronization was achieved in February 2015. However, the temporal sampling was decreased to ∼4 SLCs/year in September 2017 for crustal deformation applications in accord with the mission basic observation scenario. This resulted in only 3 non-winter ScanSAR SLCs during December 2017 and February 2020 per track, with no predicted acquisitions in this mode during 2020. Further, ALOS-2 stripmap data have never been acquired with a better temporal sampling than 2 SLCs per year per track. With such a poor temporal sampling it is currently not possible to track time-dependent processes at Cordón Caulle with L-band data. On the other hand, if another eruption were about to occur, it would not be possible to calculate a co-eruptive time series of dDEM because TDX is no longer acquiring bistatic data in this region. The alternative to construct dDEMs is to use stereo optical data like Pléiades, SPOT and WorldView, but they do not have the required temporal resolution to construct these time series (less than 6 months) and they are also limited by the clouds (*Delgado et al.*, 2019).

7.2 Coherence

The biggest drawback for a better use of InSAR at Cordoón Caulle is the coherence loss due to its alpine conditions and thick temperate rain forest that surrounds the volcano. In my experience, the coherence loss is very fast compared with vegetated volcanoes in similar environments elsewhere like Yellowstone. Depending on the year, the snow hampers the use of InSAR between 5 and 7 months, usually from mid-late May to mid-late November. Therefore, it has not been possible to measure ground deformation in the winter on top of the volcano, even with 1-day CSK interferograms (*Delgado et al.*, 2018), although ALOS-2 ScanSAR data were promising in this aspect (*Euillades et al.*, 2017). Further, small baseline interferograms can have very low coherence even in the summer. In general, the coherence loss precludes the data processing in a rigorous small baseline fashion, i.e., to use all the interferograms that share an image as reference that have a temporal baseline shorter than a given threshold, usually shorter than two months (Figure 10). Thereby advanced time series algorithms that rely on an interferometric network with good connectivity (e.g., *Yunjun et al.*, 2019) cannot be used at Cordón Caulle. The environmental conditions of the volcano and the fast deformation rates make L-band data the ideal platform to measure ground deformation. However, as described earlier the temporal resolution of ALOS-2 has always been far from ideal and it is unlikely that L-band data availability will improve until the launch of the NASA NISAR mission in 2022.

In terms of legacy data, by far the most useful ENVISAT data are from its extension mission during 2011-2012 – the only time when the mission acquired data during every overflight. This data were acquired by the IM6 beam, not the standard IM2 of the satellite nominal mission. The main differences between the IM6 extension mission data compared with that of IM2 nominal mission are a repeat period of 30 vs 35 days, HH instead of VV polarization, a look angle of 45° instead of 23° and a good orbital control for small baseline interferograms despite the orbit drift. All of these conditions resulted in acquisitions of much better quality during the extension mission than in the nominal mission (e.g., *Delgado et al.*, 2017; *Pritchard et al.*, 2018, Figure 4). The ENVISAT IM2 acquisitions were always limited by the poor orbital control at the beginning of the mission, lack of data after 2006 and the potential drawback of the VV polarization (*Pritchard et al.*, 2018) resulting in very few useful interferograms (Figure 3a-b). On the other hand, the ALOS-1 acquisition program was always far from ideal, with a temporal resolution of ∼2-3 images per track in the austral late spring, summer and early fall. Had ALOS-1 lasted for two additional months before its failure in April 2011, just two months before the eruption, the quality of the L-band co-eruptive interferograms would be excellent and coherent observations would be available near the eruptive vent.

X-band processing at Cordón Caulle is challenging and tedious due to the rapid coherence loss and large volumes of data. Therefore it is not possible to sustain the coherence in the vegetated flanks of the volcano in early fall to late summer CSK interferograms which are required to ensure the connectivity of the InSAR network (e.g., *DeGrandpre et al.*, 2019). In the absence of GPS data, the only solution I have envisioned to remove ramps and to reference the CSK interferograms to a non-deforming area is to calculate a preliminary source model inverted from good quality ascending and descending interferograms, fix the geometry of this model, invert every CSK interferogram for its source strength and a ramp and then subtract the latter to the data (*Delgado et al.*, 2016). The situation can be even more problematic due to the orbit drift of the mission, resulting in a 2 km difference in the perpendicular baseline between SLCs acquired in early 2012 and those from 2019. Further, images that are acquired a few days apart from each other can have perpendicular baselines well beyond the critical baseline. The real value of CSK in this volcano is that a descending track is the only data set that has recorded in its entirety the sequence of $\sim$1 m of uplift (Figure 5a-d). On the other hand TSX data were only acquired in a systematic way during the onset of the eruption in 2011. The coherence of these austral winter interferograms is extremely low, but they still recorded deformation. The lack of other TSX data hampers a direct comparison with the coherence of the CSK data.

The quality of the S1 data at Cordón Caulle has been less than ideal, in part due to data gaps and low coherence even in the austral summer despite the 12 day repeat period. It is also not straightforward to select summer to summer interferograms to connect the non-winter small baseline sets of interferograms (Figure 10). *Pritchard et al.*, 2018 found that the coherence of S1 is lower than the coherence of RS2 Wide Ultra Fine (WUF) interferograms because the resolution of the latter is one order of magnitude better than the resolution of the S1 TOPS mode and the RS2 HH instead of the S1 VV polarization. Despite the unrivalled benefits that S1 has provided to the volcano and active tectonics InSAR communities (e.g., *Funning and Garcia*, 2019), due to the aforementioned issues I do not consider that S1 data have significantly contributed to a better understanding of magma dynamic at Cordón Caulle. However this situation might change with the lack of ALOS-2 data, potential lack of access to RS2 data and the huge baseline drift of CSK, making S1 the most reliable source of InSAR data in the area in the future. If an eruption were to occur in the winter, it is likely that near-field measurement will only be possible with the GPS stations located on top of the volcano (Figure 5).

Considering the time scales of most of the magmatic processes at Cordón Caulle and the coherence and temporal resolution of each data, currently the best suited data to study ground deformation at this volcano are the RS2 WUF beams. However, in my experience

InSAR users should rely on the whole civilian constellation of SAR data, because each of these aforementioned platforms have several advantages and drawbacks and using all of them can improve the temporal sampling of individual platforms.

8 Conclusions

In this golden era of InSAR it is impressive how much the technology and the resulting amounts of data have evolved since the ENVISAT mission in the early 2000's leading to outstanding discoveries like the aforementioned sequence of unrest between 2003 and 2020. Many aspects remain to be elucidated from the Cordón Caulle dynamics and here is where I envision that the wealth of InSAR data that will be provided by the next generation InSAR missions (NISAR, Sentinel-1C/D, TanDEM-L, RADARSAT constellation, CSK Second Generation, SAOCOM-1A) will improve our understanding of volcano dynamics like ENVISAT and COSMO-SkyMED did at the beginning of the previous decades. I envision that many of the issues with the lack of data and coherence loss could be solved with a better collaboration between the multiple space agencies, resulting in acquisitions with higher temporal resolution and the best data characteristics (e.g., polarization) for the environmental conditions of the volcano.

In general InSAR has been an excellent tool to detect episodic pulses of ground deformation that I have related to magma injection given the lack of other constraining data and there is little doubt that the detection capability will improve with the future missions. Since Cordón Caulle has been a restless volcano for most of the whole 2003-2020 period, it is very likely than in the near future it will deform again providing new and exciting discoveries. Despite the InSAR technological advances, the geological interpretation of geodetic signals has not evolved as nearly as fast. In my opinion the most significant scientific question from a volcano geodesy perspective that must be addressed at Cordón Caulle is what magmatic and hydrothermal processes produce ground deformation signals? Geophysical data in general do not have resolution to resolve for the detailed structures of interest in plumbing systems. Therefore, I envision that more realistic models of ground deformation are required to assess whether InSAR data can be explained by models of magma injection or some other mechanism of unrest including volatile exsolution and melt reorganization inside of a crystal mush.

Acknowledgements

This review is the result of discussions and collaborations with many colleagues in the world in the past six years. I thank the French Centre National d'Etudes Spatiales (CNES) for a postdoctoral fellowship, Editor Pablo Euillades for the invitation to participate in this special issue, A. Pérez-Fodich (Institut de Physique du Globe de Paris) for suggesting the idea to write this review article, and many colleagues who in one way or the other have contributed with either data, software, ideas or comments to a better understanding of the dynamics of Cordón Caulle. These include Matthew Pritchard, Jennifer Jay, Whyjay Zheng (Cornell University), Paul Lundgren (Jet Propulsion Laboratory, Caltech/NASA), Julia Kubanek (ESTEC, European Space Agency), Kyle Anderson (California Volcano Observatory, U. S. Geological Survey), Michael Poland (Cascades Volcano Observatory, U. S. Geological Survey), Simona Zoffoli (Agenzia Spatiale Italiana), Sergey Samsonov (Canada Centre for Mapping and Earth Observation, Natural Resources Canada), Diego Coppola (Universitá di Torino), Philippe Ruprecht, Heather Winslow (University of Nevada, Reno), Helge Gonnermann, Patrick Phelps (Rice University), Carolina Muñoz (Universidad de Chile), Juliet Biggs, Fabien Albino (University of Bristol), Loreto Córdova, Daniel Basualto, Daniel Bertin, Luis Lara (SERNAGEOMIN), Tara Shreve, Raphaël Grandin (Institut de Physique du Globe de Paris), Hugh Tuffen (University of Lancaster), and Camila Novoa (Géosciences Environnement Toulouse). Finally I acknowledge the two anonymous reviewers whose comments improved the quality of this study. ENVISAT images were provided by the European Space Agency (ESA) and Level 1 SLC images are available at the ESA On-The-Fly site. ALOS-1 data are property of Japanese Aerospace Exploration Agency (JAXA) and the Japanese Ministerium of Trade and Commerce and are available at the Alaska Satellite Facility by NASA. Sentinel-1A/B SLC data were provided by ESA and distributed by Alaska Satellite Facility and CNES PEPS. TerraSAR-X data were provided by Deutsches Zentrum für Luft- und Raumfahrt (DLR) through the scientific quota available to the CEOS Latin America Volcano Pilot Project (CLAPP) coordinated by Michael Poland (USGS) and Simona Zoffoli (ASI) (*Pritchard et al.*, 2018). COSMO-SkyMED data were provided by Agenzia Spatiale Italiana (ASI) through CLAPP. RADARSAT-2 data were provided by Canadian Space Agency (CSA) and MacDonald, Dettwiler & Associates (MDA) Ltd. through CLAPP and the SOAR-EI project #5437. TanDEM-X DEMs and CoSSC data were provided by DLR through the DEM proposals #DEM_GEOL2437 and NTI_INSA0405. The GPS data were provided by OVDAS-SERNAGEOMIN and are available upon request through the Portal Transparencia platform. The processed data sets and intermediate products are available upon request to the author except for RADARSAT-2 data which are not available for open distribution under the license agreement of MDA. Several figures were created with the GMT software (*Wessel and Smith*, 1998).

Figures

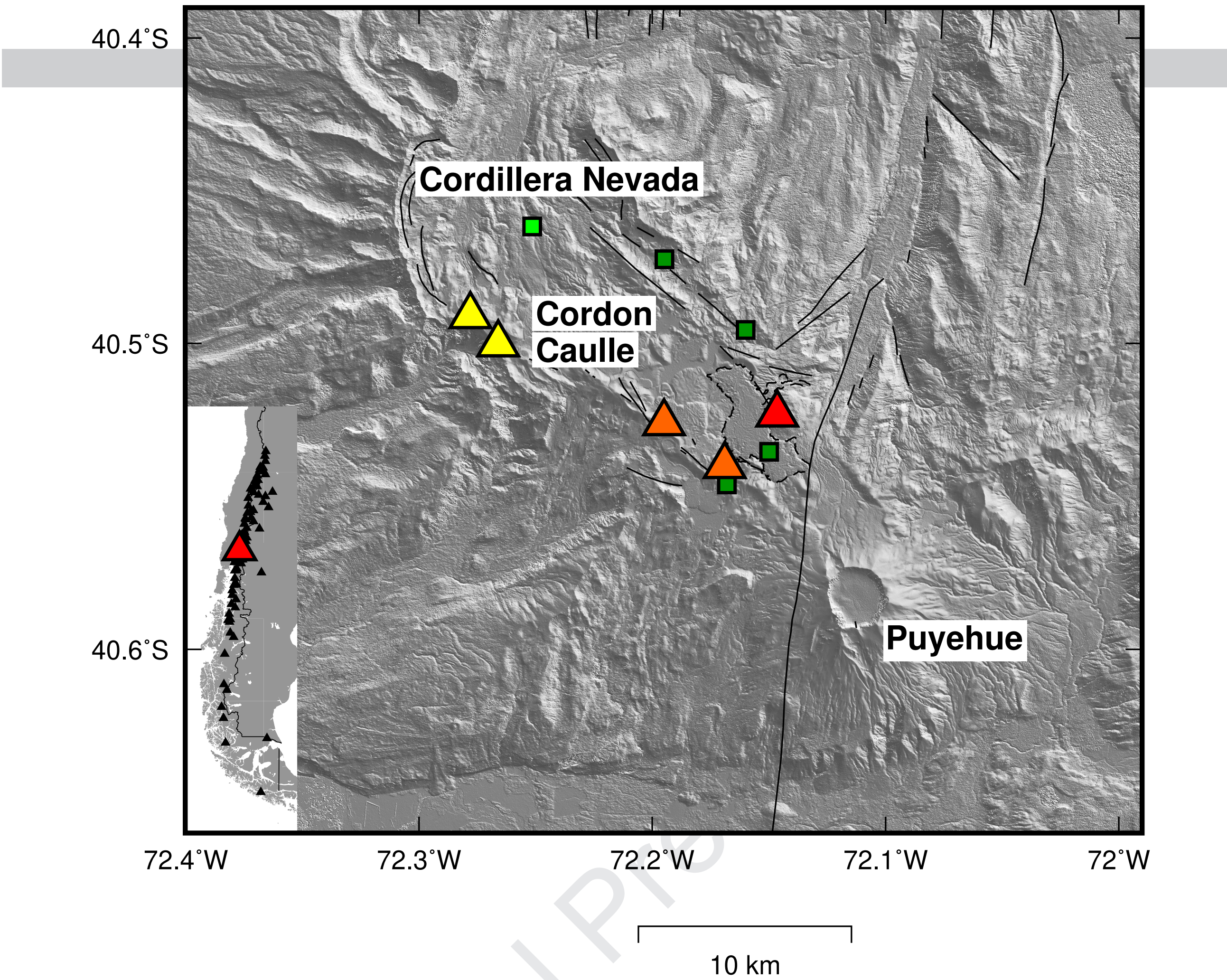

Figure 1: Cordón Caulle location map draped over the 12 m TanDEM-X shaded topography. The yellow, orange and red triangles are the 1921-1922, 1960 and 2011-2012 eruptive vents. The black dashed outline is the 2011-2012 lava flow and the black lines are faults (*Jay et al.*, 2014). Green squares are hot springs and fumaroles and the light green square is the Trahuilco geyser (*Sepulveda et al.*, 2004). All the eruptive vents are located in the NW-SE direction faults that bound the Cordón Caulle graben. The inset shows the location within South America, where the black and red triangles are Holocene volcanoes and Cordón Caulle.

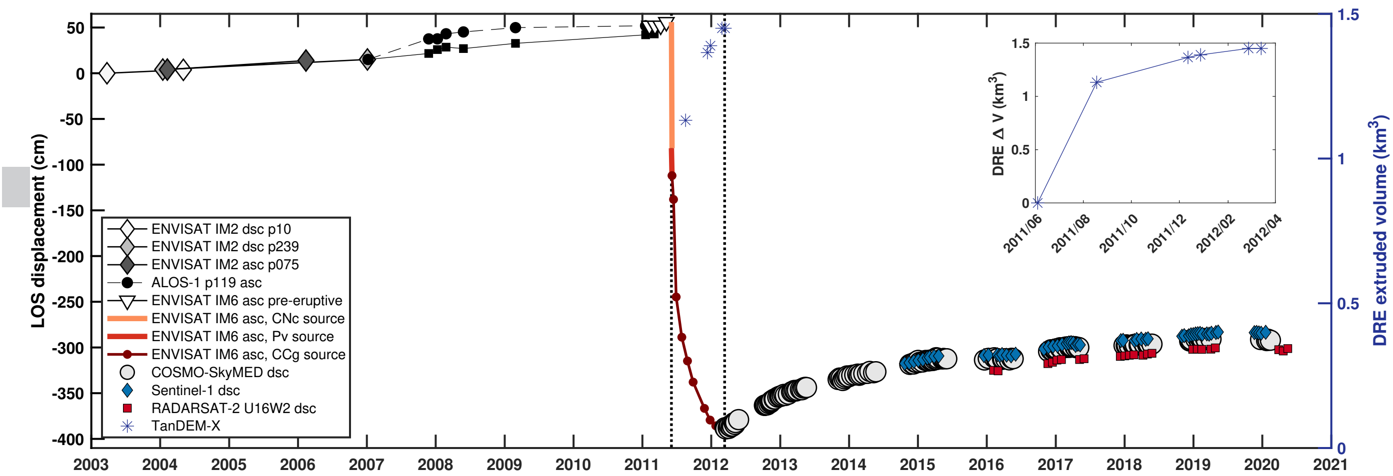

Figure 2: Compilation of line-of-sight (LOS) ground displacement from InSAR time series between 2003 and 2020 for selected pixels, including the 2011-2012 eruption (vertical dashed lines). The figure combines data from different orbits and viewing geometries because there is no single data that spans the whole sequence of unrest. The different data sets have been shifted by a constant so they lie approximately on top of each other for a better visual comparison. This also give the time series a qualitative continuity. Data location in Figure 3a-b and Figure S1 for ENVISAT IM2 (Image Mode 2) 2003-2007, Figure 3c,d for ALOS-1 2007-2011, Figure 3e for ENVISAT IM6 (Image Mode 6) pre-eruptive, Figure 4a,b for ENVISAT IM6 CNc (Cordillera Nevada caldera), Pv (Puyehue volcano) and CCg (Cordón Caulle graben) sources, Figure 6a,g,h for COSMO-SkyMED, Sentinel-1 and RADARSAT-2. Asc/dsc refers to ascending and descending data respectively. p10, p239, p075 and p119 refers to ENVISAT IM2 paths 10, 239 075 and ALOS-1 path 119. ENVISAT IM6 pre-eruptive time series by *Reath et al.*, 2019. COSMO-SkyMED, RADARSAT-2 and Sentinel-1 time series updated from *Delgado et al.*, 2018. Right axis and inset show dense rock equivalent (DRE) lava flow extruded and laccolith intruded volume from TanDEM-X differential DEMs (*Delgado et al.*, 2019). ENVISAT IM6 time series for CNc and Pv sources were calculated adding the maximum displacement produced by each one as recorded in Figure 4a. ENVISAT IM6 time series for CCg source was calculated for the point of maximum LOS predicted by the best-fit prolate spheroid model because there is no coherence on top of the volcano during more than half of the eruption (*Delgado et al.*, 2019).

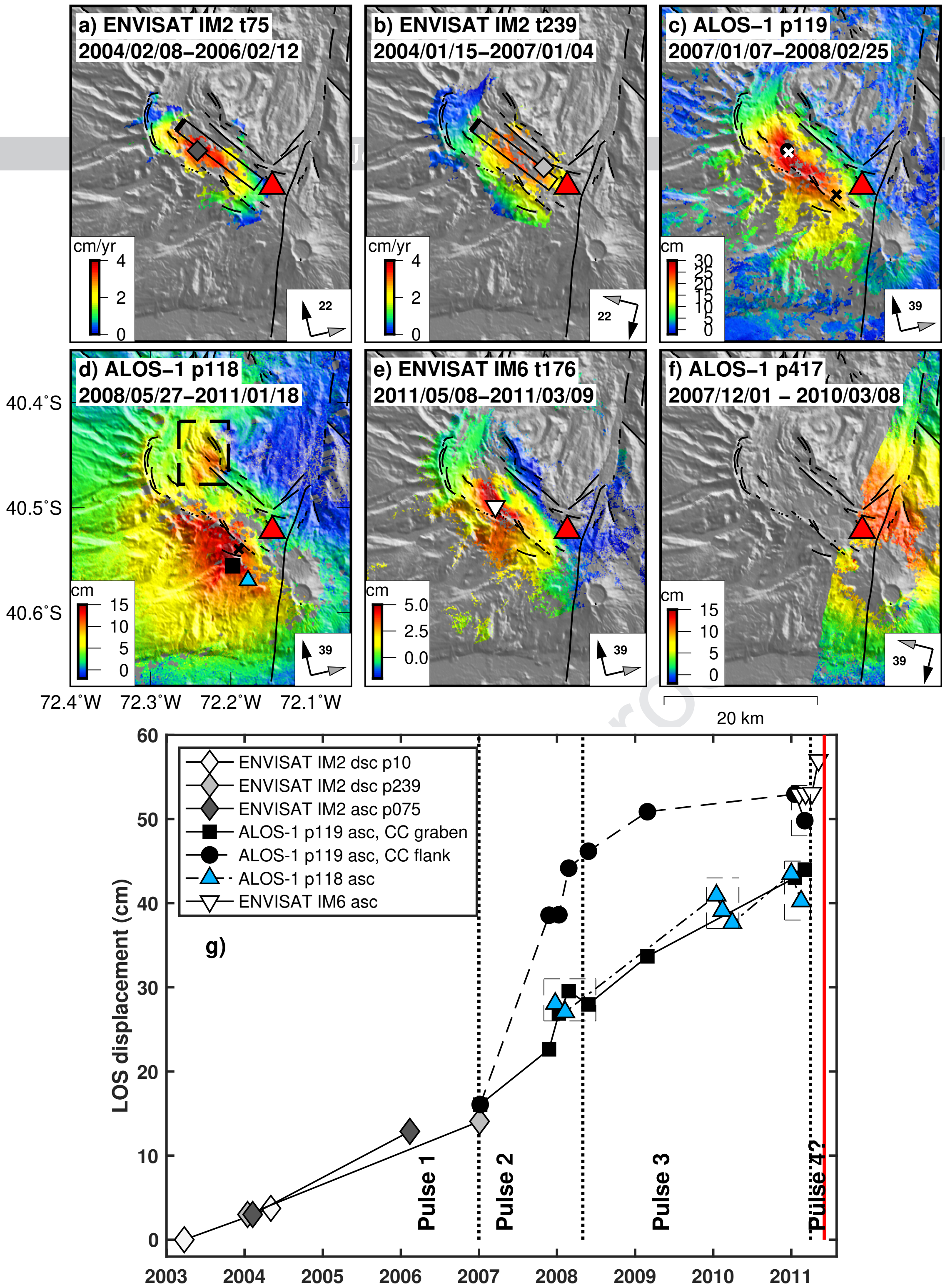

Figure 3: Summary of InSAR observations of pre-eruptive LOS uplift between 2003 and 2011. a-f). All panels show LOS ground deformation with the respective deformation sources and the 2011-2012 eruptive vent (red triangle). a-b) show interferograms converted to mean ground velocity while c-f) show the cumulative ground deformation. In each panel the black and grey arrows show the satellite heading and horizontal component of the LOS vector. The number next to the arrows is the look angle. a-b) First pulse of uplift during 2003-2007 with a rate of ∼3-4 cm/yr. The black square is the contour of the best-fit sill model. c) Second pulse of uplift during 2007-2008 with a total displacement of ∼30 cm. The crosses show the best-fit Mogi sources. d, f) Third pulse of uplift during 2008-2011 with a total displacement of ∼15 cm. The dashed line is the area near the Trahuilco geyser in February - March 2010 that uplifted likely triggered by the 2010 Maule earthquake. The cross shows the best-fit pressurized Mogi source. e) Potential fourth pulse of uplift during early 2011 with a total displacement of ∼5 cm. f) Descending ALOS-1 interfeorgrams that shows the end of the second pulse of uplift and the third pulse of uplift. g). Time series of ground deformation calculated for the pixels of the same color and symbol in the upper panel and Figure 2. The time series were shifted by an arbitrary constant as in Figure 2. Rate map for ALOS-1 p118 asc is not shown in the figure. ENVISAT IM6 time series for early 2011 by *Reath et al.*, 2019. The dashed lines show localized atmospheric signals that are non-stationary across the scene, and therefore cannot be corrected with an empirical correction that correlates the phase and the topography across the interferogram.

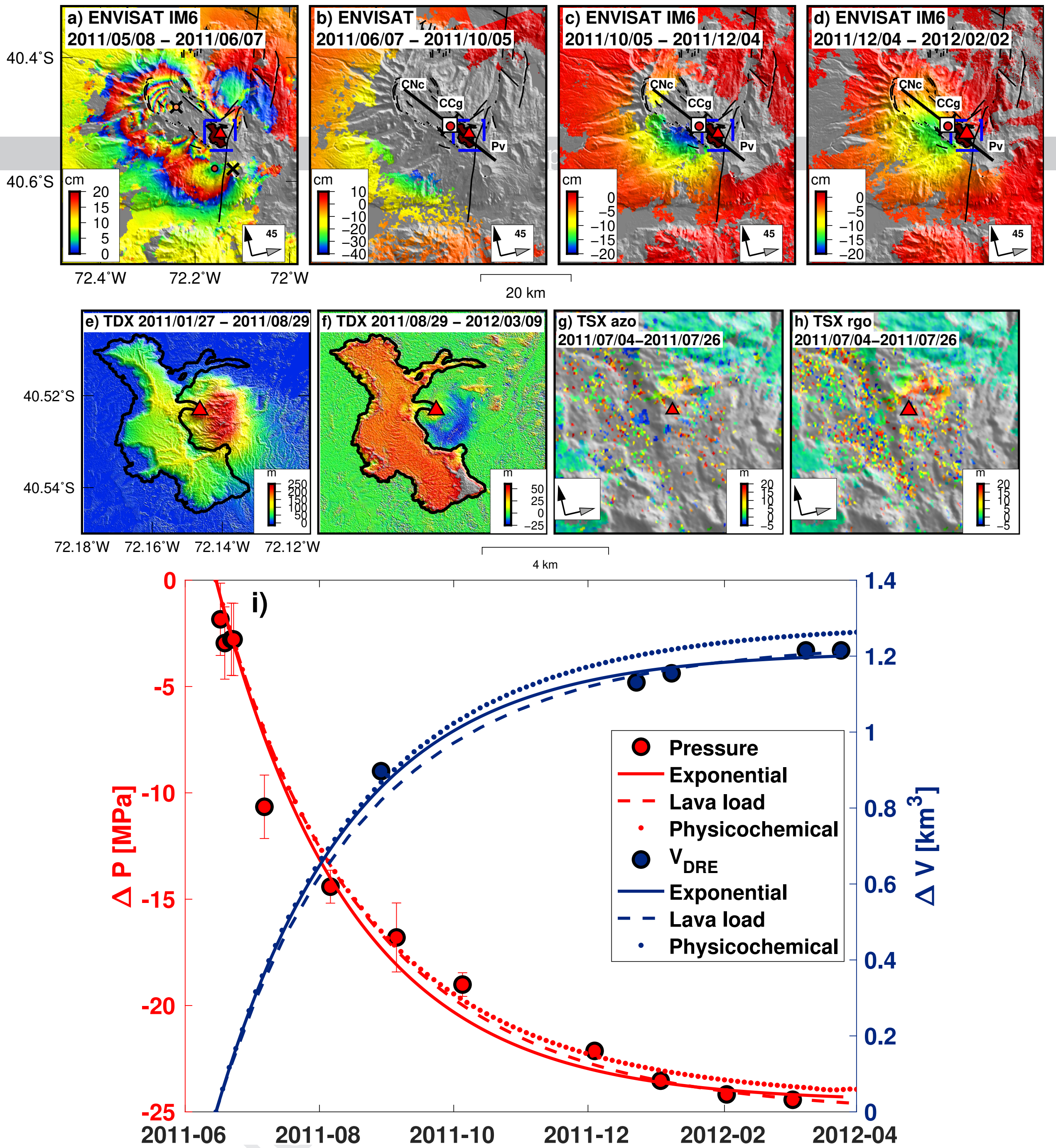

Figure 4: Summary of InSAR observations of subsidence during the 2011-2012 eruption. a-d) Ground subsidence recorded by four ENVISAT interferograms. The data span the first three days of the eruption (a) (modified from *Jay et al.*, 2014), day three to 4 months (b) (modified from *Jay et al.*, 2014), four to six months (c), six to eight months (d). Interferogram a) is presented wrapped with one fringe equivalent to 20 cm of ground deformation to highlight ∼1.3 m and ∼0.3 m of subsidence at Cordillera Nevada caldera (CNc) and Puyehue volcano (Pv). The best-fit Mogi sources for a) are the two black crosses circles and the best-fit Yang source for b-d) is the white square with the black thick lines that show the spheroid semi-major and minor axes. The circles in a) and the red circle in b-d) show the location of the time series in Figure 2. The red triangle is the eruptive vent. The dashed blue square shows the area of e-h). TanDEM-X differential DEMs that span from the beginning of the eruption to August 2011 (e) and August 2011 to March 2012 (f). Azimuth (azo, g) and range offsets (rgo,h) that record more than 10 m of post-emplacement deformation in the area of the shallow laccolith. i) Time series of pressure drop (red circles) and intruded laccolith and extruded lava flow volume (blue circles) during the effusive phase of the eruption with fits for three different eruption models (modified from Figure 8 of *Delgado et al.*, 2019). Here exponential refers to an analytic model of reservoir depressurization and lava effusion whose solution is an exponential function (Equation 1-Equation 2). Lava load is a numerical model that incorporates the effects of the lava load onto the reservoir force balance (*Mastin et al.*, 2008). Physicochemical is a numerical model that incorporates both the lava load effect and the H_2O and CO_2 exsolution in the reservoir (*Anderson and Segall*, 2013; *Delgado et al.*, 2019).

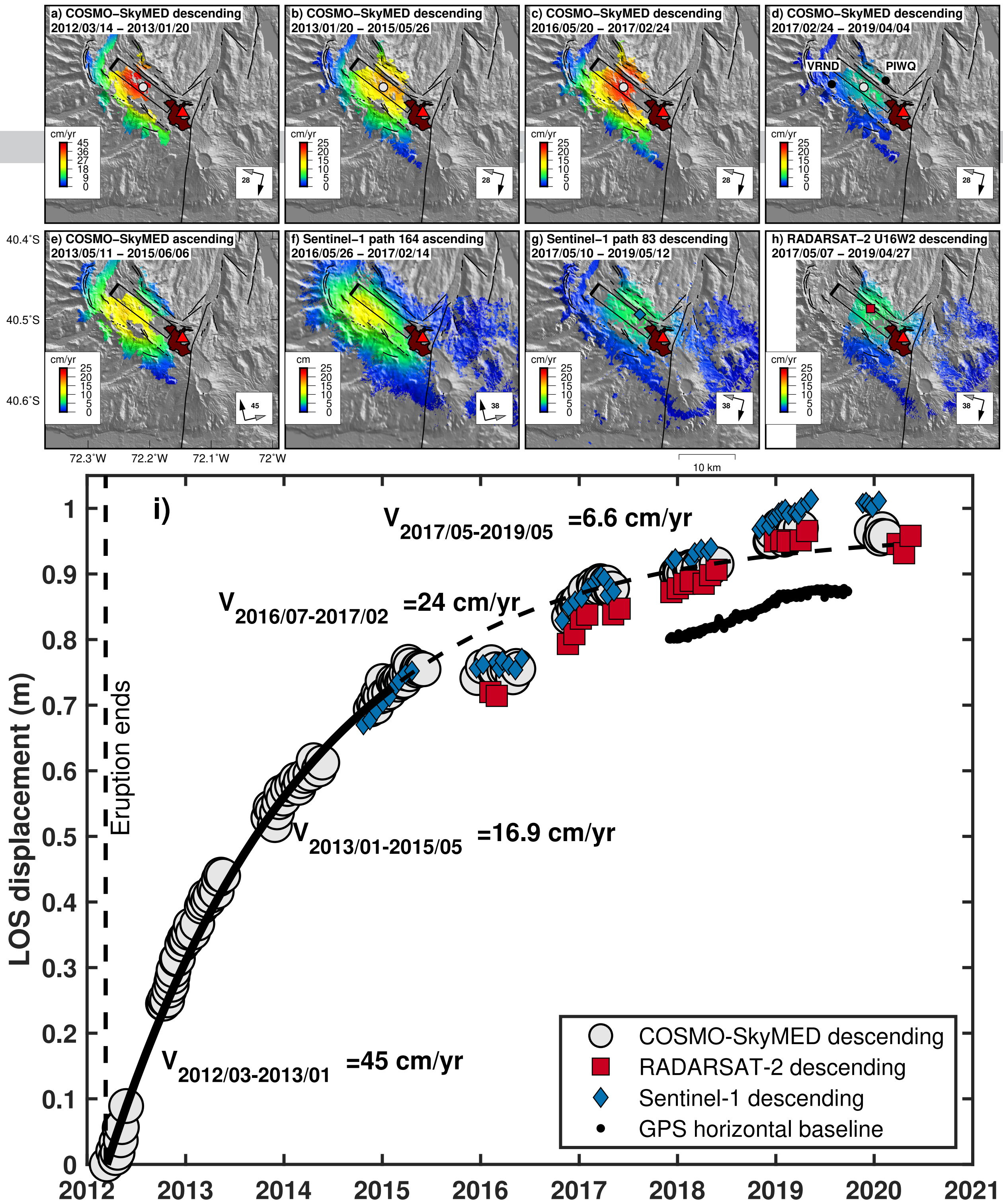

Figure 5: Summary of InSAR observations of post-eruptive LOS ground uplift between 2012 and 2020. Mean ground velocity recorded by a-d) CSK descending 2012-2019, e) CSK ascending 2013-2015, f) S1 ascending 2016-2017, g) S1 descending 2017-2019 and h) RS2 descending 2017-2019. Data in a,b,e) from *Delgado et al.*, 2016 and data in c,f) modified from *Delgado et al.*, 2018. d,g,h) show new data. Note that c) and f) cover the same time span, but are plot with different color scales because c) is a mean velocity and f) shows the cumulative displacement during the 6 months of this uplift event. The black rectangle is the best-fit tensile dislocation with uniform opening during the 2012-2017 time span (*Delgado et al.*, 2016). The black circles in d) are the GPS stations installed in December 2017. The brown outline and the red triangle are the 2011-2012 lava flow and eruptive vent respectively. i) Descending time series of ground deformation for selected pixels for CSK (grey circles in a-d), S1 (blue diamond in g) and RS2 (red square in h). The data shows three pulses of uplift during March 2012 - May 2015, July 2016 - February 2017 and May 2017 - May 2020. The data sets have been shifted by an arbitrary constant so they approximately lie on top of each other to simplify the geologic interpretation. The GPS data are the horizontal baseline change between the two stations located on both sides of the volcano (d). The black thick line is an exponential fit to the 2012-2015 CSK data and is indicative of magma injection. The dashed black line is the exponential fit to the 2012-2015 CSK data extrapolated until 2020.

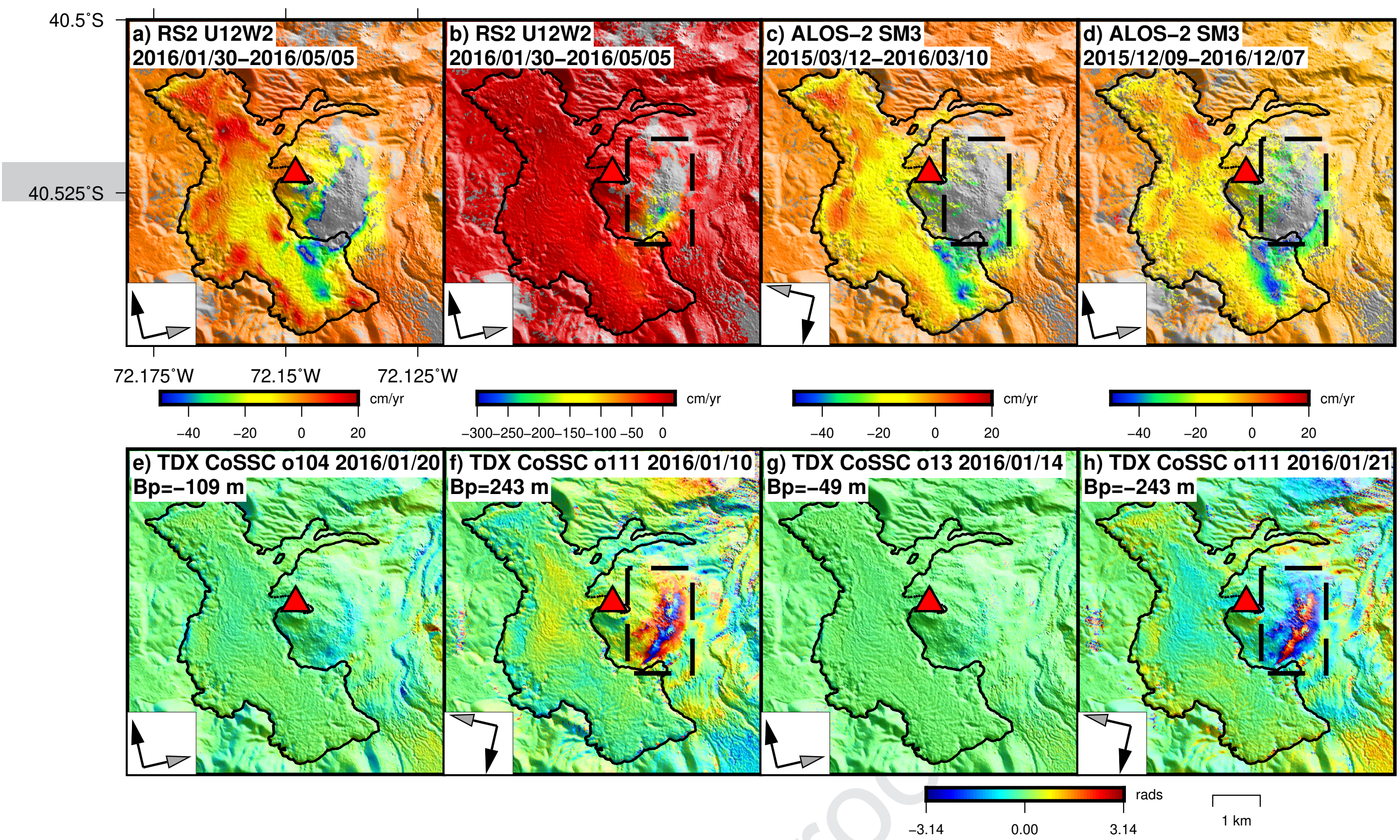

Figure 6: a-d) Mean ground velocity at the lava flow during a period with no deformation of magmatic origin. a-b) Mean ground velocity from a RADARSAT-2 Wide Ultra Fine 12 stack during February - May 2016. a) and b) show the same data but with different color scales to highlight deformation in the lava flow and in the laccolith respectively. The dashed black box shows the area of the laccolith. c-d) ALOS-2 SM3 interferograms that span one year showing mean ground velocity. e-h) TanDEM-X differential bistatic interferograms with the reference topographic phase removed with the 12m TanDEM-X DEM from 2011-2014. Here B_p is the perpendicular baseline. The dashed black box shows the area of the laccolith with a DEM error which propagates into subsidence with a high rate of 3 m/yr in the RS2 stack. The black and grey arrows show the satellite heading and LOS direction. The red triangle is the 2011 eruptive vent. The black thick line is the lava flow contour (*Bertin et al.*, 2015).

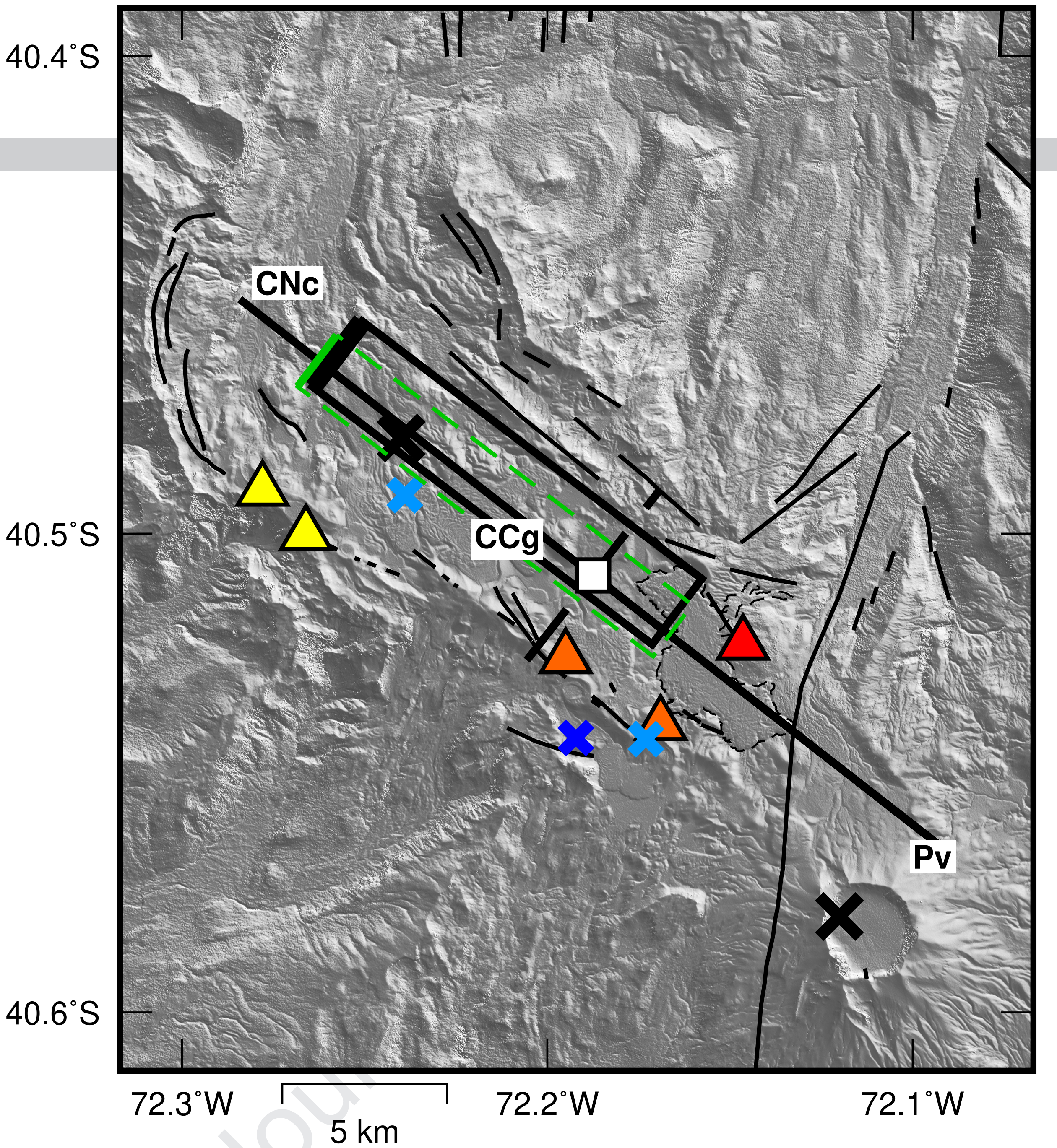

Figure 7: Compilation of deformation sources derived from InSAR inversions on top of TanDEM-X topography. The yellow, orange and red triangles are the 1921-1922, 1960 and 2011-2012 eruptive vents. The thin dashed outline is the 2011-2012 lava flow. The green rectangle is the 2003-2007 Okada source model (Figure 3, Figure S1), the light blue crosses are the 2007-2008 Mogi source model (*Jay et al.*, 2014), the blue cross is the 2008-2011 Mogi source model (*Jay et al.*, 2014), the black crosses are the Mogi sources for the first three days of the eruption (*Jay et al.*, 2014), the white square, thick black line and dashed black lines are the centroid, semi major- and semi-minor axes of the spheroid source model during the rest of the eruption (Figure 4, *Delgado et al.*, 2019), and the black square is the 2012-2017 Okada source model (Figure 5, *Delgado et al.*, 2018, 2016). The black lines are faults (*Jay et al.*, 2014)

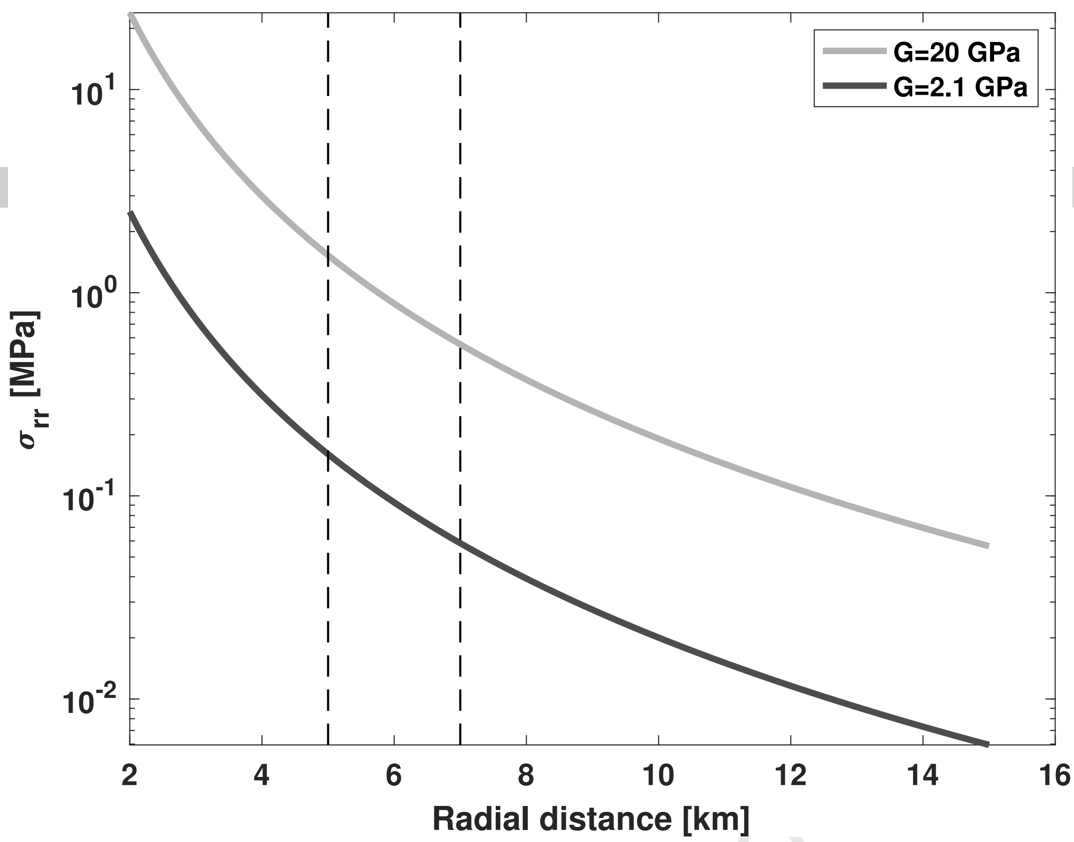

Figure 8: Radial stress (Equation 4) produced by a volume change of 0.03 km^3 in the deformation source active during the 2008-2011 episode of uplift as a function of radial distance and shear modulii (G=2.1 MPa from *Heap et al.*, 2020 and G=20 MPa from *Delgado et al.*, 2019). Dashed lines show the range of distance between the 2008-2011 and the coeruptive deformation sources. The figure shows that the volume change can increase the radial stress 0.08-2 MPa on distances similar to those between the pre and co-eruptive deformation sources. See main text for details.

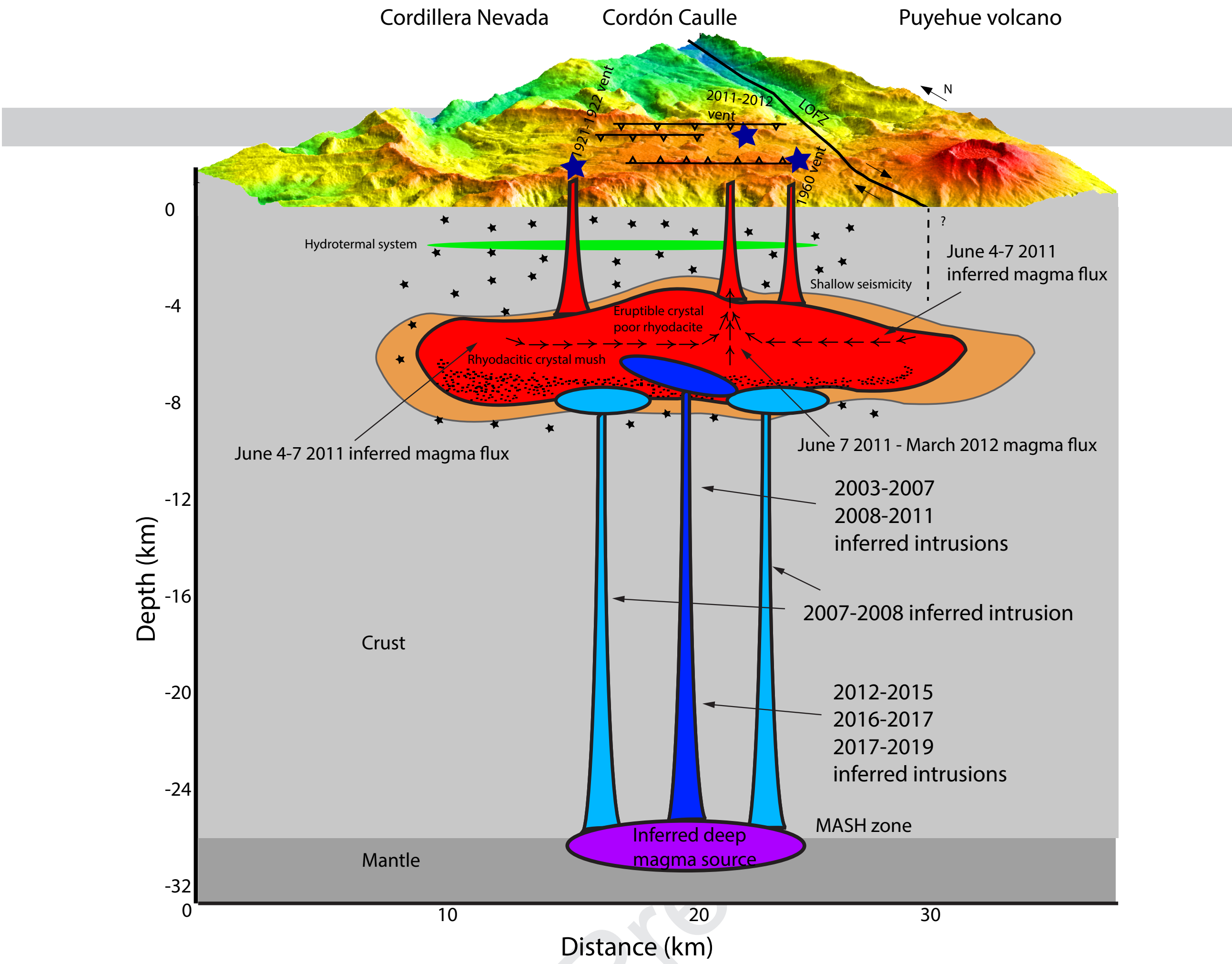

Figure 9: Cordón Caulle geological cross section (updated from *Delgado et al.*, 2016, 2018) that summarizes the estimated deformation sources between 2003–2011, 2011-2012 and 2012–2019 derived from InSAR modeling and the inferred magma sources of the 1921–1922, 1960, and 2011–2012 eruptions from geobarometry (*Lara et al.*, 2006a; *Singer et al.*, 2008; *Castro et al.*, 2013; *Jay et al.*, 2014). The red region is the hypothetical mush zone, likely surrounded by a viscoelastic shell (orange region). The storage region could also be a collection of discrete, connected reservoirs instead of a large, interconnected zone. Black points in the red regions show crystals that might have settled at the bottom of the reservoir, thus reducing the magma viscosity (*Castro et al.*, 2013) and enhancing interstitial liquid extraction, a condition likely required to produce eruptible magma in a silicic magma chamber (*Bachmann and Bergantz*, 2008; *Cooper*, 2017). The light blue regions show the inferred magma intrusion during 2007-2008, the blue region shows the inferred magma sources during 2003-2007, 2008-2011, 2012–2015, 2016-2017 and 2018-2019, and the green region is the hydrothermal system beneath the volcano (*Sepulveda et al.*, 2004; *Sepulveda et al.*, 2007). Blue stars show the location of the historical eruptive vents, black stars are earthquakes beneath the volcano (*Delgado et al.*, 2016; *Wendt et al.*, 2017), horizontal lines with open triangles show the graben bounding faults, and LOFZ is the Liquiñe-Ofqui regional fault zone that crosses the volcano (*Lara et al.*, 2006b). MASH zone refers to a hypothetical zone of magma melting, assimilation, storage, and homogenization (*Hildreth and Moorbath*, 1988) that I infer to be the source of magmas (see rationale in *Jay et al.*, 2014). The sketch shows that the source of the 1921–1922, 1960, and 2011–2012 eruptions is the same reservoir located beneath Cordillera Nevada, Cordón Caulle, and Puyehue volcanoes and where magma intruded during 2003-2007, 2007–2008, 2008-2011, 2012–2015, 2016-2017 and 2017-2019. InSAR data are interpreted to show that magma flowed from the Cordillera Nevada and Puyehue volcanoes towards the 2011-2012 eruptive event during the first three eruption days and then flowed from the same area where magma injection occurred afterwards. Note that the shape of the crystal mush is hypothetical because no geophysical imaging is available for the volcano.

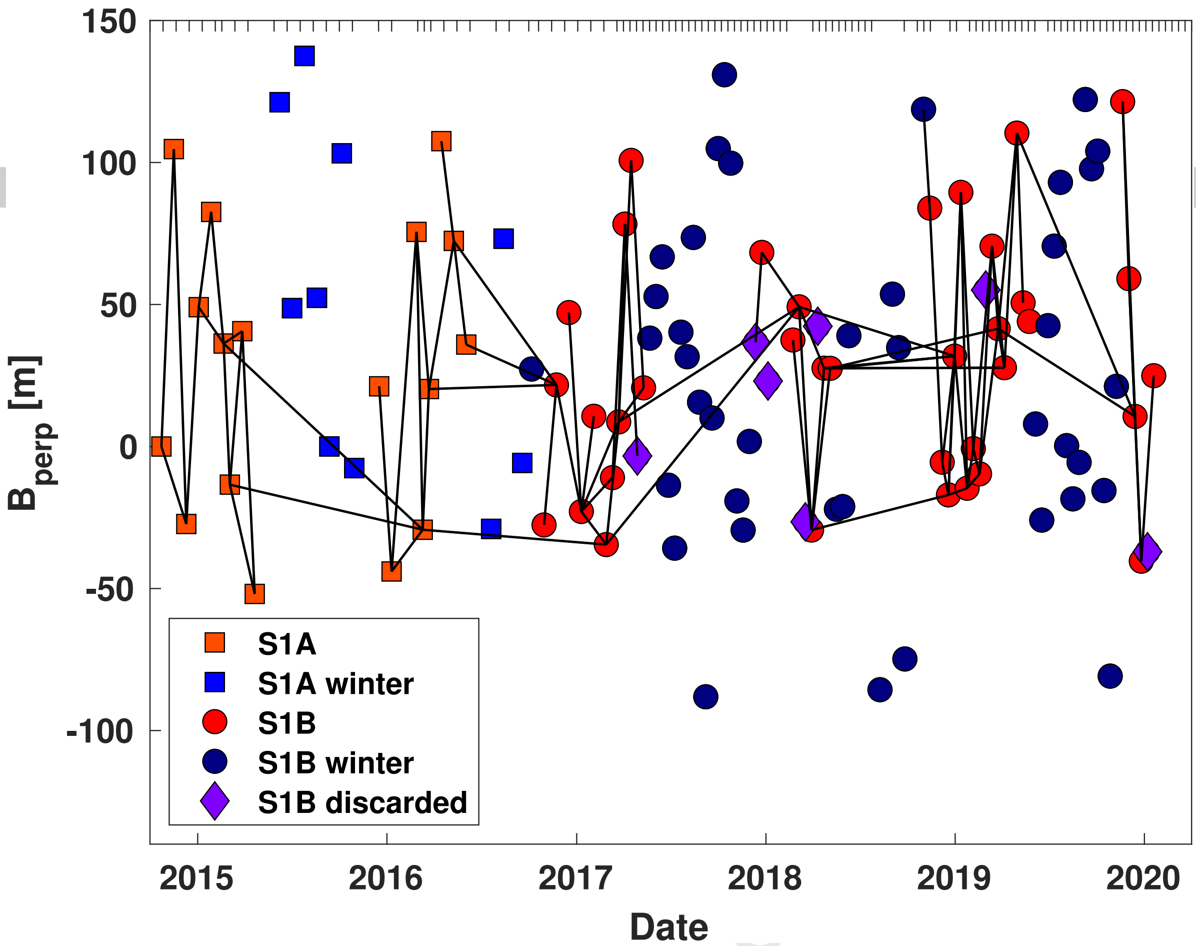

Figure 10: Perpendicular baseline (B_{perp}) plot for S1 SLCs from descending track 83. The time series for this track is in Figure 5g. Ticks on top of the figure show the date of the images, and clearly show the onset of 12 days acquisitions in February 2017 and several periods with data gaps. Blue squares and circles are SLCs acquired under winter conditions with snow on top of the volcano and purple circles are summer and early fall SLCs that result in interferograms with coherence loss either on top or on the vegetated flanks of the volcano. Black lines are interferograms used in the time series. The figure shows that despite the 12 day repeat period of the mission since February 2017, a significant amount of the small baseline interferograms are not useful due to their low coherence, even in the austral summer. Coherence loss was a severe problem during February 2017 - May 2018 but not as much during May 2018 - May 2019. Also, it is not straightforward to select summer to summer interferograms to ensure the connectivity of the InSAR network.

References

Albino, F., and F. Sigmundsson (2014), Stress transfer between magma bodies: Influence of intrusions prior to 2010 eruptions at Eyjafjallajokull volcano, Iceland, *Journal of Geophysical Research-Solid Earth*, *119*(4), 2964–2975, doi:10.1002/2013jb010510.

Albino, F., V. Pinel, and F. Sigmundsson (2010), Influence of surface load variations on eruption likelihood: application to two Icelandic subglacial volcanoes, Grimsvotn and Katla, *Geophysical Journal International*, *181*(3), 1510–1524, doi:10.1111/j.1365-246X.2010.04603.x.

Alloway, B. V., N. J. G. Pearce, G. Villarosa, V. Outes, and P. I. Moreno (2015), Multiple melt bodies fed the AD 2011 eruption of Puyehue-Cordon Caulle, Chile, *Scientific Reports*, *5*, doi:10.1038/srep17589.

Anderson, K., and P. Segall (2011), Physics-based models of ground deformation and extrusion rate at effusively erupting volcanoes, *Journal of Geophysical Research-Solid Earth*, *116*, doi:10.1029/2010jb007939.

Anderson, K., and P. Segall (2013), Bayesian inversion of data from effusive volcanic eruptions using physics-

Satellite	λ [cm]	Dates (yyyy/mm/dd)	Pass	Path	θ	Mode	Beam	Pixel Size [m]	# SAR	Volcanic process
ENVISAT	5.6	2003/03/25-2006/12/19	D	10	22	SM	IM2	20	9	Pre-eruptive uplift
ENVISAT	5.6	2003/04/10-2009/04/23	D	239	22	SM	IM2	20	9	Pre-eruptive uplift
ENVISAT	5.6	2003/02/04-2010/04/13	A	304	22	SM	IM2	20	20	Pre-eruptive uplift
ENVISAT	5.6	2004/01/04-2010/03/28	A	75	22	SM	IM2	20	5	Pre-eruptive uplift
ALOS-1	23.8	2007/02/05-2011/02/16	A	118	38	SM	FBD, FBS	10	10	Pre-eruptive uplift
ALOS-1	23.8	2007/01/07-2011/03/05	A	119	38	SM	FBD, FBS	10	10	Pre-eruptive uplift
ALOS-1	23.8	2007/12/01-2010/03/08	D	417	38	SM	FBD, FBS	10	5	Pre-eruptive uplift
ENVISAT	5.6	2011/02/07-2012/03/03	A	176	40	SM	IM6	12	13	Co-eruptive subsidence
TerraSAR-X	3.1	2011/06/06-2011/06/17	A	13	47	SM	strip_016	2	2	Co-eruptive subsidence
TerraSAR-X	3.1	2011/06/08-2011/06/19	D	35	46	SM	strip_015	2	2	Co-eruptive subsidence
TerraSAR-X	3.1	2011/06/11-2011/06/22	A	89	57	SM	strip_024	2	2	Co-eruptive subsidence
TerraSAR-X	3.1	2011/06/18-2011/06/29	A	28	17	SM	strip_002	2	2	Co-eruptive subsidence
RADARSAT-2	5.5	2011/12/03-2012/02/13	D	N/A	31	SM	WLMF23	5	4	Co-eruptive subsidence
TanDEM-X	3.1	2011/01/27-2012/03/25	D	35, 111	46,33	SM	46,32	2	6	Lava effusion
TanDEM-X	3.1	2016/01/10-2016/01/21	D, A, A	111, 13, 104	33,48,33	SM	N/A	2	4	DEM error analysis
COSMO-SkyMED	3.1	2012/03/14-2020/02/13	D	N/A	28	SM	HIMAGE H4-02	2	189	Post-eruptive uplift
COSMO-SkyMED	3.1	2013/05/11-2016/01/29	A	N/A	28	SM	HIMAGE H4-02	2	37	Post-eruptive uplift
UAVSAR	23.8	2013/03/27-2015/03/30	D	N/A	23-68	SM	N/A	7	3	Post-eruptive uplift
RADARSAT-2	5.5	2012/12/21-2017/03/30	D	N/A	38	SM	WF02	8	14	Post-eruptive uplift
RADARSAT-2	5.5	2016/01/30-2019/04/20	A	N/A	38	SM	U12W2	2	21	Post-eruptive uplift
RADARSAT-2	5.5	2016/02/06-2020/05/15	D	N/A	43	SM	U16W2	2	26	Post-eruptive uplift
Sentinel-1	5.5	2015/01/08-2019/05/17	A	164	36	TOPS	IW	20	55	Post-eruptive uplift
Sentinel-1	5.5	2014/10/23-2020/01/19	D	083	38	TOPS	IW	20	60	Post-eruptive uplift
ALOS-2	24	2015/12/09-2017/11/22	A	036	35	SM	FBD	10	3	Post-eruptive uplift
ALOS-2	24	2015/03/12-2018/05/03	D	130	34	SM	FBD	10	7	Post-eruptive uplift
ALOS-2	24	2015/02/21-2017/02/18	D	129	N/A	ScanSAR	WD1	60	18	Post-eruptive uplift

Table 1: Details of the processed SAR images for interferometry and DEM generation (*Jay et al.*, 2014; *Bignami et al.*, 2014; *Delgado et al.*, 2016, 2018, 2019; *Wendt et al.*, 2017; *Euillades et al.*, 2017, this study). This table is not exhaustive and does not include all the existing SAR data. They do not include the data sets used for pixel tracking (Figure 4). Winter images (June 5 to October 15) have not been included in this compilation of data except for the co-eruptive ENVISAT data and for ALOS-2 ScanSAR. The columns show the satellite name, radar wavelength (λ), date range (year/month/day), whether the satellite is in an ascending (A) or descending (D) orbit, satellite path if available, average incidence angle (θ), radar mode, radar beam if available, number of synthetic aperture radar images (SAR) per track and the ground pixel size. SM is stripmap, FBD/FBS are the fine beam double/single polarization beams of ALOS-1 (14 and 28 MHz), SM3 is the stripmap beam of ALOS-2, HIMAGE is the SM mode of COSMO-SkyMED, TOPS is Terrain Observation by Progressive Scans, IW is Interferometric Wide Swath. The RADARSAT-2 beams for which data are available at Cordón Caulle are Wide Fine 2 (WF02), Wide Ultra Fine 12 and 16 (U12W2/U16W2) and Wide Multi Look Fine 23 (WLMF23). N/A refers to a information not available, like the RS2 and CSK path numbers.

based models: Application to Mount St. Helens 2004-2008, *Journal of Geophysical Research-Solid Earth*, *118*(5), 2017–2037, doi:10.1002/jgrb.50169.

Astort, A., T. R. Walter, F. Ruiz, L. Sagripanti, A. Nacif, G. Acosta, and A. Folguera (2019), Unrest at Domuyo Volcano, Argentina, Detected by Geophysical and Geodetic Data and Morphometric Analysis, *Remote Sensing*, *11*(18), 2175, doi:10.3390/rs11182175.

Bachmann, O., and G. Bergantz (2008), The magma reservoirs that feed supereruptions, *Elements*, *4*(1), 17–21, doi:10.2113/gselements.4.1.17.

Bachmann, O., and G. W. Bergantz (2006), Gas percolation in upper-crustal silicic crystal mushes as a mechanism for upward heat advection and rejuvenation of near-solidus magma bodies, *Journal of Volcanology and Geothermal Research*, doi:10.1016/j.jvolgeores.2005.06.002.

Bachmann, O., and C. Huber (2016), Silicic magma reservoirs in the Earth's crust, *American Mineralogist*, *101*(11), 2377–2404, doi:10.2138/am-2016-5675.

Barrientos, S. E. (1994), Large thrust earthquakes and volcanic eruptions, *Pure and Applied Geophysics*, *142*(1), 225–237, doi:10.1007/bf00875972.

Bathke, H., M. Shirzaei, and T. R. Walter (2011), Inflation and deflation at the steep-sided Llaima stratovolcano (Chile) detected by using InSAR, *Geophysical Research Letters*, *38*, doi:10.1029/2011gl047168.

Bato, M. G., V. Pinel, Y. Yan, F. Jouanne, and J. Vandemeulebrouck (2018), Possible deep connection between volcanic systems evidenced by sequential assimilation of geodetic data, *Scientific Reports*, *8*(1), 11,702, doi:10.1038/s41598-018-29811-x.

Bertin, D., L. E. Lara, D. Basualto, Á. Amigo, C. Cardona, L. Franco, F. Gil, and J. Lazo (2015), High effusion rates of the Cordón Caulle 2011–2012 eruption (Southern Andes) and their relation with the quasi-harmonic tremor, *Geophysical Research Letters*, *42*(17), 7054–7063, doi:10.1002/2015GL064624.

Biggs, J., and C. Annen (2019), The lateral growth and coalesence of magma systems, *Philosophical Transactions of the Royal Society A: Mathematical, Physical and Engineering Sciences*, *377*(2139), 20180,005, doi:10.1098/rsta.2018.0005.

Biggs, J., and M. E. Pritchard (2017), Global Volcano Monitoring: What Does It Mean When Volcanoes Deform?, *Elements*, *13*(1), 17–22, doi:10.2113/gselements.13.1.17.

Biggs, J., Z. Lu, T. Fournier, and J. T. Freymueller (2010), Magma flux at Okmok Volcano, Alaska, from a joint inversion of continuous GPS, campaign GPS, and interferometric synthetic aperture radar, *Journal of Geophysical Research-Solid Earth*, *115*, doi:10.1029/2010jb007577.

Biggs, J., S. K. Ebmeier, W. P. Aspinall, Z. Lu, M. E. Pritchard, R. S. J. Sparks, and T. A. Mather (2014), Global link between deformation and volcanic eruption quantified by satellite imagery, *Nature Communications*, *5*, doi:10.1038/ncomms4471.

Biggs, J., E. Robertson, and K. Cashman (2016), The lateral extent of volcanic interactions during unrest and eruption, *Nature Geoscience*, doi:10.1038/ngeo2658.

Bignami, C., S. Corradini, L. Merucci, M. de Michele, D. Raucoules, G. De Astis, S. Stramondo, and J. Piedra (2014), Multisensor Satellite Monitoring of the 2011 Puyehue-Cordon Caulle Eruption, *Ieee Journal of Selected Topics in Applied Earth Observations and Remote Sensing*, *7*(7), 2786–2796, doi:10.1109/jstars.2014.2320638.

Bonadonna, C., M. Pistolesi, R. Cioni, W. Degruyter, M. Elissondo, and V. Baumann (2015), Dynamics of wind-affected volcanic plumes: The example of the 2011 Cordón Caulle eruption, Chile, *Journal of Geophysical Research: Solid Earth*, *120*(4), 2242–2261, doi:10.1002/2014JB011478.

Browning, J., K. Drymoni, and A. Gudmundsson (2015), Forecasting magma-chamber rupture at Santorini volcano, Greece, *Scientific Reports*, *5*(15785), doi:10.1038/srep15785.

Carn, S. A., L. Clarisse, and A. J. Prata (2016), Multi-decadal satellite measurements of global volcanic degassing, *Journal of Volcanology and Geothermal Research*, *311*, 99–134, doi:10.1016/j.jvolgeores.2016.01.002.

Carrara, A., V. Pinel, P. Bascou, E. Chaljub, and S. De la Cruz-Reyna (2019), Post-emplacement dynamics of andesitic lava flows at Volcán de Colima, Mexico, revealed by radar and optical remote sensing data, *Journal of Volcanology and Geothermal Research*, doi:10.1016/j.jvolgeores.2019.05.019.

Carrier, A., J. L. Got, A. Peltier, V. Ferrazzini, T. Staudacher, P. Kowalski, and P. Boissier (2015), A damage model for volcanic edifices: Implications for edifice strength, magma pressure, and eruptive processes, *Journal of Geophysical Research: Solid Earth*, doi:10.1002/2014JB011485.

Cashman, K. V., R. S. J. Sparks, and J. D. Blundy (2017), Vertically extensive and unstable magmatic systems: A unified view of igneous processes, *Science*, doi:10.1126/science.aag3055.

Castro, J. M., C. I. Schipper, S. P. Mueller, A. S. Militzer, A. Amigo, C. S. Parejas, and D. Jacob (2013), Storage and eruption of near-liquidus rhyolite magma at Cordon Caulle, Chile, *Bulletin of Volcanology*, *75*(4), 17, doi:10.1007/s00445-013-0702-9.

Castro, J. M., I. N. Bindeman, H. Tuffen, and C. I. Schipper (2014), Explosive origin of silicic lava: Textural and delta D-H2O evidence for pyroclastic degassing during rhyolite effusion, *Earth and Planetary Science Letters*, *405*, 52–61, doi:10.1016/j.epsl.2014.08.012.

Castro, J. M., B. Cordonnier, C. I. Schipper, H. Tuffen, T. S. Baumann, and Y. Feisel (2016), Rapid laccolith intrusion driven by explosive volcanic eruption, *Nature Communications*, *7*, doi:10.1038/ncomms13585.

Castruccio, A., M. Diez, and R. Gho (2017), The Influence of Plumbing System Structure on Volcano Dimensions and Topography, *Journal of Geophysical Research: Solid Earth*, pp. n/a–n/a, doi:10.1002/2017JB014855.

Cembrano, J., and L. Lara (2009), The link between volcanism and tectonics in the southern volcanic zone of the Chilean Andes: A review, *Tectonophysics*, *471*(1-2), 96–113, doi:10.1016/j.tecto.2009.02.038.

Chang, W.-L., R. B. Smith, C. Wicks, J. M. Farrell, and C. M. Puskas (2007), Accelerated uplift and magmatic intrusion of the Yellowstone caldera, 2004 to 2006, *Science*, *318*(5852), 952–956, doi:10.1126/science.1146842.

Chaussard, E. (2016), Subsidence in the Parícutin lava field: Causes and implications for interpretation of deformation fields at volcanoes, *Journal of Volcanology and Geothermal Research*, doi:10.1016/j.jvolgeores.2016.04.009.

Chouet, B. A., and R. S. Matoza (2013), A multi-decadal view of seismic methods for detecting precursors of magma movement and eruption, *Journal of Volcanology and Geothermal Research*, *252*, 108–175, doi:10.1016/j.jvolgeores.2012.11.013.

Cooper, K. M. (2017), What Does a Magma Reservoir Look Like? The "Crystal's-Eye" View, *Elements*, *13*(1), 23–28, doi:10.2113/gselements.13.1.23.

Cooper, K. M., and A. J. Kent (2014), Rapid remobilization of magmatic crystals kept in cold storage, *Nature*, doi:10.1038/nature12991.

Coppola, D., M. Laiolo, A. Franchi, F. Massimetti, C. C., and L. E. Lara (2017), Measuring effusion rates of obsidian lava flows by means of satellite thermal data, *Journal of Volcanology and Geothermal Research*, doi:10.1016/j.jvolgeores.2017.09.003.

DeGrandpre, K. G., J. D. Pesicek, Z. Lu, H. R. DeShon, and D. C. Roman (2019), High Rates of Inflation During a Noneruptive Episode of Seismic Unrest at Semisopochnoi Volcano, Alaska in 2014–2015, *Geochemistry, Geophysics, Geosystems*, *n/a*(n/a), doi:10.1029/2019GC008720.

Degruyter, W., and C. Huber (2014), A model for eruption frequency of upper crustal silicic magma chambers, *Earth and Planetary Science Letters*, *403*, 117–130, doi:10.1016/j.epsl.2014.06.047.

Delgado, F. (2018), Magma storage, transport and eruption dynamics in the Southern Andean Volcanic Zone imaged with InSAR geodesy, Ph.D. thesis, Cornell University.

Delgado, F., M. Pritchard, R. Lohman, and J. A. Naranjo (2014), The 2011 Hudson volcano eruption (Southern Andes, Chile): Pre-eruptive inflation and hotspots observed with InSAR and thermal imagery, *Bulletin of Volcanology*, *76*(5), 19, doi:10.1007/s00445-014-0815-9.

Delgado, F., M. E. Pritchard, D. Basualto, J. Lazo, L. Cordova, and L. E. Lara (2016), Rapid reinflation following the 2011-2012 rhyodacite eruption at Cordon Caulle volcano (Southern Andes) imaged by InSAR: Evidence for magma reservoir refill, *Geophysical Research Letters*, *43*(18), 9552–9562, doi:10.1002/2016gl070066.

Delgado, F., M. Pritchard, S. Ebemier, P. Gonzalez, and L. Lara (2017), Recent unrest (2002-2015) imaged by space geodesy at the highest risk Chilean volcanoes: Villarrica, Llaima, and Calbuco (Southern Andes), *Journal of Volcanology and Geothermal Research*, *344*, 270–288, doi:10.1016/j.jvolgeores.2017.05.020.

Delgado, F., M. Pritchard, S. Samsonov, and L. Córdova (2018), Renewed post-eruptive uplift following the 2011-2012 rhyolitic eruption of Cordón Caulle (Southern Andes, Chile): evidence for transient episodes of magma reservoir recharge during 2012-2018, *Journal of Geophysical Research: Solid Earth*, doi:10.1029/2018JB016240.

Delgado, F., J. Kubanek, K. Anderson, P. Lundgren, and M. Pritchard (2019), Physicochemical models of effusive rhyolitic eruptions constrained with InSAR and DEM data: A case study of the 2011-2012 Cordón Caulle eruption, *Earth and Planetary Science Letters*, *524*, 115,736, doi:10.1016/J.EPSL.2019.115736.

Derrien, A., N. Villeneuve, A. Peltier, and F. Beauducel (2015), Retrieving 65 years of volcano summit deformation from multitemporal structure from motion: The case of Piton de la Fournaise (La Réunion Island), *Geophysical Research Letters*, doi:10.1002/2015GL064820.

Doin, M.-P., F. Lodge, S. Guillaso, R. Jolivet, C. Lasserre, G. Ducret, R. Grandin, E. Pathier, and V. Pinel (2011), Presentation of the small baseline NSBAS processing chain on a case example: the Etna deformation monitoring from 2003 to 2010 using Envisat data, in *Proceedings of the ESA Fringe Workshop*.

Dufek, J., C. Huber, and L. Karlstrom (2012), Magma chamber dynamics and thermodynamics, in *Modeling Volcanic Processes The Physics and Mathematics of Volcanism*, edited by S. A. Fagents, T. K. P. Gregg, and R. M. C. Lopes, pp. 5–31, Cambridge University Press.

Dumont, S., F. Sigmundsson, M. M. Parks, V. J. P. Drouin, G. B. M. Pedersen, I. Jónsdóttir, Á. Höskuldsson, A. Hooper, K. Spaans, M. Bagnardi, M. T. Gudmundsson, S. Barsotti, K. Jónsdóttir, T. Högnadóttir, E. Magnússon, Á. R. Hjartardóttir, T. Dürig, C. Rossi, and B. Oddsson (2018), Integration of SAR Data

Into Monitoring of the 2014–2015 Holuhraun Eruption, Iceland: Contribution of the Icelandic Volcanoes Supersite and the FutureVolc Projects, *Frontiers in Earth Science*, *6*, 231, doi:10.3389/feart.2018.00231.

Dzierma, Y., and H. Wehrmann (2012), On the likelihood of future eruptions in the Chilean Southern Volcanic Zone: interpreting the past century's eruption record based on statistical analyses, *Andean Geology*, *39*(3), 380–393, doi:10.5027/andgeoV39n3-a02.

Dzurisin, D., and Z. Lu (2007), Interferometric synthetic-aperture radar (InSAR), in *Volcano Deformation*, edited by D. Dzurisin, chap. 5, pp. 153–194, Springer, Berlin, Heidelberg, doi:10.1007/978-3-540-49302-0_5.

Dzurisin, D., C. W. Wicks, and M. P. Poland (2012), History of surface displacements at the Yellowstone Caldera, Wyoming, from leveling surveys and InSAR observations, 1923–2008, *U.S. Geological Survey Professional Paper*, *1788*, 68 p.

Dzurisin, D., Z. Lu, M. P. Poland, and C. W. Wicks (2019), Space-Based Imaging Radar Studies of U.S. Volcanoes, *Frontiers in Earth Science*, *6*, 249, doi:10.3389/feart.2018.00249.

Ebmeier, S. K., J. Biggs, T. A. Mather, J. R. Elliott, G. Wadge, and F. Amelung (2012), Measuring large topographic change with InSAR: Lava thicknesses, extrusion rate and subsidence rate at Santiaguito volcano, Guatemala, *Earth and Planetary Science Letters*, *335*, 216–225, doi:10.1016/j.epsl.2012.04.027.

Edmonds, M., and P. J. Wallace (2017), Volatiles and Exsolved Vapor in Volcanic Systems, *Elements*, *13*(1), 29–34, doi:10.2113/gselements.13.1.29.

Eineder, M. (2003), Efficient simulation of SAR interferograms of large areas and of rugged terrain, *IEEE Transactions on Geoscience and Remote Sensing*, doi:10.1109/TGRS.2003.811692.

Euillades, P. A., L. D. Euillades, M. H. Blanco, M. L. Velez, P. Grosse, and G. J. Sosa (2017), Co-eruptive subsidence and post-eruptive uplift associated with the 2011–2012 eruption of Puyehue-Cordón Caulle, Chile, revealed by DInSAR, *Journal of Volcanology and Geothermal Research*, doi:10.1016/j.jvolgeores.2017.06.023.

Farquharson, J. I., M. R. James, and H. Tuffen (2015), Examining rhyolite lava flow dynamics through photo-based 3D reconstructions of the 2011-2012 lava flowfield at Cordon-Caulle, Chile, *Journal of Volcanology and Geothermal Research*, *304*, 336–348, doi:10.1016/j.jvolgeores.2015.09.004.

Feigl, K. L., H. Le Mével, S. T. Ali, L. Cordova, N. L. Andersen, C. DeMets, and B. S. Singer (2014), Rapid uplift in Laguna del Maule volcanic field of the Andean Southern Volcanic zone (Chile) 2007-2012, *Geophysical Journal International*, *196*(2), 885–901, doi:10.1093/gji/ggt438.

Fink, J. (1980), Surface folding and viscosity of rhyolite flows, *Geology*, doi:10.1130/0091-7613(1980)8<250:SFAVOR>2.0.CO;2.

Fournier, T. J., M. E. Pritchard, and S. N. Riddick (2010), Duration, magnitude, and frequency of subaerial volcano deformation events: New results from Latin America using InSAR and a global synthesis, *Geochemistry Geophysics Geosystems*, *11*, 29, doi:10.1029/2009gc002558.

Fukushima, Y., V. Cayol, P. Durand, and D. Massonnet (2010), Evolution of magma conduits during the 1998-2000 eruptions of Piton de la Fournaise volcano, Reunion Island, *Journal of Geophysical Research-Solid Earth*, *115*, doi:10.1029/2009jb007023.

Funning, G. J., and A. Garcia (2019), A systematic study of earthquake detectability using Sentinel-1 InterferometricWide-Swath data, *Geophysical Journal International*, doi:10.1093/gji/ggy426.

Gansecki, C., R. L. Lee, T. Shea, S. P. Lundblad, K. Hon, and C. Parcheta (2019), The tangled tale of Kilauea{\textquoteright}s 2018 eruption as told by geochemical monitoring, *Science*, *366*(6470), doi:10.1126/science.aaz0147.

Gerlach, D. C., F. A. Frey, H. Moreno-Roa, and L. Lopez-Escobar (1988), Recent volcanism in the Puyehue-Cordón Caulle region, southern Andes, Chile (40.5S): Petrogenesis of evolved lavas, *Journal of Petrology*, *29*(2), 333–382, doi:10.1093/petrology/29.2.333.

Gonnermann, H. M. (2015), Magma Fragmentation, *Annual Review of Earth and Planetary Sciences, Vol 43*, *43*, 431–458, doi:10.1146/annurev-earth-060614-105206.

Gonnermann, H. M., and M. Manga (2012), Dynamics of magma ascent in the volcanic conduit, in *Modeling Volcanic Processes The Physics and Mathematics of Volcanism*, edited by S. A. Fagents, T. K. P. Gregg, and R. M. C. Lopes, pp. 55–84, Cambridge University Press.

Grandin, R. (2015), Interferometric Processing of SLC Sentinel-1 TOPS Data, in *Proceedings of the ESA Fringe Workshop*.

Head, M., J. Hickey, J. Gottsmann, and N. Fournier (2019), The Influence of Viscoelastic Crustal Rheologies on Volcanic Ground Deformation: Insights From Models of Pressure and Volume Change, *Journal of Geophysical Research: Solid Earth*, doi:10.1029/2019JB017832.

Heap, M. J., M. Villeneuve, F. Albino, J. I. Farquharson, E. Brothelande, F. Amelung, J. L. Got, and P. Baud (2020), Towards more realistic values of elastic moduli for volcano modelling, *Journal of Volcanology and Geothermal Research*, doi:10.1016/j.jvolgeores.2019.106684.

Henderson, S. T., and M. E. Pritchard (2013), Decadal volcanic deformation in the Central Andes Volcanic Zone revealed by InSAR time series, *Geochemistry Geophysics Geosystems*, *14*(5), 1358–1374, doi:10.1002/ggge.20074.

Hildreth, W., and S. Moorbath (1988), Crustal contributions to arc magmatism in the Andes of Central Chile, *Contributions to Mineralogy and Petrology*, *98*(4), 455–489, doi:10.1007/bf00372365.

Hooper, A. J. (2008), A multi-temporal InSAR method incorporating both persistent scatterer and small baseline approaches, *Geophysical Research Letters*, doi:10.1029/2008GL034654.

Hotta, K., M. Iguchi, T. Ohkura, T. Hendrasto, H. Gunawan, U. Rosadi, and E. Kriswati (2017), Magma intrusion and effusion at Sinabung volcano, Indonesia, from 2013 to 2016, as revealed by continuous GPS observation, *Journal of Volcanology and Geothermal Research*, doi:doi.org/10.1016/j.jvolgeores.2017.12.015.

Huber, C., O. Bachmann, and J. Dufek (2010), The limitations of melting on the reactivation of silicic mushes, *Journal of Volcanology and Geothermal Research*, doi:10.1016/j.jvolgeores.2010.06.006.

Huber, C., O. Bachmann, and J. Dufek (2011), Thermo-mechanical reactivation of locked crystal mushes: Melting-induced internal fracturing and assimilation processes in magmas, *Earth and Planetary Science Letters*, doi:10.1016/j.epsl.2011.02.022.

Huber, C., O. Bachmann, and J. Dufek (2012), Crystal-poor versus crystal-rich ignimbrites: A competition between stirring and reactivation, *Geology*, doi:10.1130/G32425.1.

Huber, C., M. Townsend, W. Degruyter, and O. Bachmann (2019), Optimal depth of subvolcanic magma chamber growth controlled by volatiles and crust rheology, *Nature Geoscience*, doi:10.1038/s41561-019-0415-6.

Hurwitz, S., L. B. Christiansen, and P. A. Hsieh (2007), Hydrothermal fluid flow and deformation in large calderas: Inferences from numerical simulations, *Journal of Geophysical Research-Solid Earth*, *112*(B2), doi:10.1029/2006jb004689.

Jaupart, C. (2000), Magma ascent at shallow levels, in *Encyclopedia of Volcanoes*, edited by H. Sigurdsson, pp. 237–245, Academic Press, San Diego.

Jaupart, C., and S. Tait (1990), Dynamics of eruptive phenomena, *Reviews in Mineralogy*, *24*, 213–238.

Jay, J., F. Costa, M. Pritchard, L. Lara, B. Singer, and J. Herrin (2014), Locating magma reservoirs using InSAR and petrology before and during the 2011-2012 Cordon Caulle silicic eruption, *Earth and Planetary Science Letters*, *403*, 463, doi:10.1016/j.epsl.2014.07.021.

Kubanek, J., M. Westerhaus, and B. Heck (2017), TanDEM-X Time Series Analysis Reveals Lava Flow Volume and Effusion Rates of the 2012–2013 Tolbachik, Kamchatka Fissure Eruption, *Journal of Geophysical Research: Solid Earth*, pp. n/a–n/a, doi:10.1002/2017JB014309.

Lara, L. E., J. A. Naranjo, and H. Moreno (2004), Rhyodcacitic fissure eruption in Southern Andes (Cordon Caulle; 40.5 degrees S) after the 1960 (Mw : 9.5) Chilean earthquake: a structural interpretation, *Journal of Volcanology and Geothermal Research*, *138*(1-2), 127–138, doi:10.1016/j.jvolgeores.2004.06.009.

Lara, L. E., H. Moreno, J. A. Naranjo, S. Matthews, and C. P. de Arce (2006a), Magmatic evolution of the Puyehue-Cordon Caulle volcanic complex (40 degrees S), Southern Andean Volcanic Zone: From shield to unusual rhyolitic fissure volcanism, *Journal of Volcanology and Geothermal Research*, *157*(4), 343–366, doi:10.1016/j.jvolgeores.2006.04.010.

Lara, L. E., A. Lavenu, J. Cembrano, and C. Rodriguez (2006b), Structural controls of volcanism in transversal chains: Resheared faults and neotectonics in the Cordon Caulle-Puyehue area (40.5 degrees S), Southern Andes, *Journal of Volcanology and Geothermal Research*, *158*(1-2), 70–86, doi:10.1016/j.jvolgeores.2006.04.017.

Le Mével, H., K. L. Feigl, L. Córdova, C. DeMets, and P. Lundgren (2015), Evolution of unrest at Laguna del Maule volcanic field (Chile) from InSAR and GPS measurements, 2003 to 2014, *Geophysical Research Letters*, *42*(16), 6590–6598, doi:10.1002/2015GL064665.

Le Mével, H., P. Gregg, and K. L. Feigl (2016), Magma injection into a long-lived reservoir to explain geodetically measured uplift: application to the 2007–2014 unrest episode at Laguna del Maule volcanic field, Chile, *Journal of Geophysical Research: Solid Earth*, pp. n/a–n/a, doi:10.1002/2016JB013066.

Lengline, O., D. Marsan, J. L. Got, V. Pinel, V. Ferrazzini, and P. G. Okubo (2008), Seismicity and deformation induced by magma accumulation at three basaltic volcanoes, *Journal of Geophysical Research-Solid Earth*, *113*(B12), 12, doi:10.1029/2008jb005937.

Lev, E., P. Ruprecht, C. Oppenheimer, N. Peters, M. Patrick, P. A. Hernández, L. Spampinato, and J. Marlow (2019), A global synthesis of lava lake dynamics, *Journal of Volcanology and Geothermal Research*, doi:10.1016/j.jvolgeores.2019.04.010.

Liao, Y., S. A. Soule, and M. Jones (2018), On the Mechanical Effects of Poroelastic Crystal Mush in Classical Magma Chamber Models, *Journal of Geophysical Research: Solid Earth*, doi:10.1029/2018JB015985.

Lowenstern, J. B., T. W. Sisson, and S. Hurwitz (2017), Probing magma reservoirs to improve volcano forecasts, *EOS*, *98*, doi:doi.org/10.1029/2017EO085189.

Lu, Z., and D. Dzurisin (2010), Ground surface deformation patterns, magma supply, and magma storage at Okmok volcano, Alaska, from InSAR analysis: 2. Coeruptive deflation, July-August 2008, *Journal of Geophysical Research-Solid Earth*, *115*, doi:10.1029/2009jb006970.

Lu, Z., and D. Dzurisin (2014), InSAR Imaging of Aleutian Volcanoes, in *InSAR Imaging of Aleutian Volcanoes*, Springer-Verlag Berlin Heidelberg, doi:10.1007/978-3-642-00348-6_6.

Lu, Z., D. Dzurisin, J. Biggs, C. Wicks, and S. McNutt (2010), Ground surface deformation patterns, magma supply, and magma storage at Okmok volcano, Alaska, from InSAR analysis: 1. Intereruption deformation, 1997-2008, *Journal of Geophysical Research-Solid Earth*, *115*, doi:10.1029/2009jb006969.

Lundgren, P., M. Nikkhoo, S. V. Samsonov, P. Milillo, F. Gil-Cruz, and J. Lazo (2017), Source model for the Copahue volcano magma plumbing system constrained by InSAR surface deformation observations, *Journal of Geophysical Research-Solid Earth*, *122*(7), 5729–5747, doi:10.1002/2017jb014368.

Lundgren, P., M. Bagnardi, and H. Dietterich (2019), Topographic Changes During the 2018 Kīlauea Eruption From Single-Pass Airborne InSAR, *Geophysical Research Letters*, p. 2019GL083501, doi:10.1029/2019GL083501.

Lundgren, P., T. Girona, M. G. Bato, V. J. Realmuto, S. Samsonov, C. Cardona, L. Franco, E. Gurrola, and M. Aivazis (2020), The dynamics of large silicic systems from satellite remote sensing observations: the intriguing case of Domuyo volcano, Argentina, *Scientific Reports*, *10*(1), 11,642, doi:10.1038/s41598-020-67982-8.

MacQueen, P., F. Delgado, K. Reath, M. E. Pritchard, M. Bagnardi, P. Milillo, P. Lundgren, O. Macedo, V. Aguilar, M. Ortega, R. Anccasi, I. Lazarte, and R. Miranda (2020), Volcano-tectonic interactions at Sabancaya volcano, Peru: eruptions, magmatic inflation, moderate earthquakes, and fault creep, *Journal of Geophysical Research*, doi:10.1029/2019JB019281.

Magnall, N., M. R. James, H. Tuffen, and C. Vye-Brown (2017), Emplacing a cooling-limited rhyolite lava flow: similarities with basaltic lava flows, *Frontiers in Earth Science*, *5*(44), doi:10.3389/feart.2017.00044.

Major, J. J., and L. E. Lara (2013), Overview of Chaiten Volcano, Chile, and its 2008-2009 eruption, *Andean Geology*, *40*(2), 196–215, doi:10.5027/andgeoV40n2-a01.

Manga, M., I. Beresnev, E. E. Brodsky, J. E. Elkhoury, D. Elsworth, S. E. Ingebritsen, D. C. Mays, and C. Y. Wang (2012), Changes in permeability caused by transient stresses: Field observations, experiments, and mechanisms, *Reviews of Geophysics*, doi:10.1029/2011RG000382.

Mastin, L. G., E. Roeloffs, N. M. Beeler, and J. E. Quick (2008), Constraints on the size, overpressure, and volatile content of the Mount St. Helens magma system from geodetic and dome-growth measurements during the 2004–2006+ eruption, in *A volcano rekindled; the renewed eruption of Mount St. Helens, 2004-2006*, vol. 1750, edited by D. R. Sherrod, W. E. Scott, and P. H. Stauffer, p. 856, U.S. Geological Survey Professional Paper.

Miller, C. A., H. Le Mevel, G. Currenti, G. Williams-Jones, and B. Tikoff (2017), Microgravity changes at the Laguna del Maule volcanic field: Magma-induced stress changes facilitate mass addition, *Journal of Geophysical Research-Solid Earth*, *122*(4), 3179–3196, doi:10.1002/2017jb014048.

Montgomery-Brown, E. K., C. W. Wicks, P. F. Cervelli, J. O. Langbein, J. L. Svarc, D. R. Shelly, D. P. Hill, and M. Lisowski (2015), Renewed inflation of Long Valley Caldera, California (2011 to 2014), *Geophysical Research Letters*, *42*(13), 5250–5257, doi:10.1002/2015gl064338.

Morgado, E., D. J. Morgan, J. Harvey, M.-Á. Parada, A. Castruccio, R. Brahm, F. Gutiérrez, B. Georgiev, and S. J. Hammond (2019), Localised heating and intensive magmatic conditions prior to the 22–23 April 2015 Calbuco volcano eruption (Southern Chile), *Bulletin of Volcanology*, *81*(4), 24, doi:10.1007/s00445-019-1280-2.

Nakada, S., A. Zaennudin, M. Yoshimoto, F. Maeno, Y. Suzuki, N. Hokanishi, H. Sasaki, M. Iguchi, T. Ohkura, H. Gunawan, and H. Triastuty (2017), Growth process of the lava dome/flow complex at Sinabung Volcano during 2013–2016, *Journal of Volcanology and Geothermal Research*, doi:10.1016/j.jvolgeores.2017.06.012.

National Academies of Sciences and Medicine, E. (2017), *Volcanic Eruptions and Their Repose, Unrest, Precursors, and Timing.*, The National Academies Press, Washington, DC, doi:doi.org/10.17226/24650.

Nikkhoo, M., T. R. Walter, P. R. Lundgren, and P. Prats-Iraola (2016), Compound dislocation models (CDMs) for volcano deformation analyses, *Geophysical Journal International*, doi:10.1093/gji/ggw427.

Novoa, C., D. Remy, M. Gerbault, J. Baez, A. Tassara, L. Cordova, C. Cardona, M. Granger, S. Bonvalot, and F. Delgado (2019), Viscoelastic relaxation: A mechanism to explain the decennial large surface displacements at the Laguna del Maule silicic volcanic complex, *Earth and Planetary Science Letters*, *521*, 46–59, doi:10.1016/J.EPSL.2019.06.005.

Pallister, J. S., A. K. Diefenbach, W. C. Burton, J. Munoz, J. P. Griswold, L. E. Lara, J. B. Lowenstern, and C. E. Valenzuela (2013), The Chaiten rhyolite lava dome: Eruption sequence, lava dome volumes, rapid effusion rates and source of the rhyolite magma, *Andean Geology*, *40*(2), 277–294, doi:10.5027/andgeoV40n2-a06.

Papale, P., C. P. Montagna, and A. Longo (2017), Pressure evolution in shallow magma chambers upon buoyancy-driven replenishment, *Geochemistry, Geophysics, Geosystems*, doi:10.1002/2016GC006731.

Pedersen, G. B. M., J. M. C. Belart, E. Magnússon, O. K. Vilmundardóttir, F. Kizel, F. S. Sigurmundsson, G. Gísladóttir, and J. A. Benediktsson (2018), Hekla Volcano, Iceland, in the 20th Century: Lava Volumes, Production Rates, and Effusion Rates, *Geophysical Research Letters*, *45*(4), 1805–1813, doi:10.1002/2017GL076887.

Pedersen, R., and F. Sigmundsson (2006), Temporal development of the 1999 intrusive episode in the Eyjafjallajokull volcano, Iceland, derived from InSAR images, *Bulletin of Volcanology*, *68*(4), 377–393, doi:10.1007/s00445-005-0020-y.

Peltier, A., N. Villeneuve, V. Ferrazzini, S. Testud, T. Hassen Ali, P. Boissier, and P. Catherine (2018), Changes in the Long-Term Geophysical Eruptive Precursors at Piton de la Fournaise: Implications for the Response Management, *Frontiers in Earth Science*, doi:10.3389/feart.2018.00104.

Pina-Gauthier, M., L. E. Lara, K. Bataille, A. Tassara, and J. C. Baez (2013), Co-eruptive deformation and dome growth during the 2008-2009 Chaiten eruption, Southern Andes, *Andean Geology*, *40*(2), 310–323, doi:10.5027/andgeoV40n2-a08.

Pinel, V., and C. Jaupart (2003), Magma chamber behavior beneath a volcanic edifice, *Journal of Geophysical Research-Solid Earth*, *108*(B2), doi:10.1029/2002jb001751.

Pinel, V., M. P. Poland, and A. Hooper (2014), Volcanology: lessons learned from Synthetic Aperture Radar imagery, *Journal of Volcanology and Geothermal Research*, *289*, 81–113, doi:10.1016/j.jvolgeores.2014.10.010.

Pistolesi, M., R. Cioni, C. Bonadonna, M. Elissondo, V. Baumann, A. Bertagnini, L. Chiari, R. Gonzales, M. Rosi, and L. Francalanci (2015), Complex dynamics of small-moderate volcanic events: the example of the 2011 rhyolitic Cordon Caulle eruption, Chile, *Bulletin of Volcanology*, *77*(1), doi:10.1007/s00445-014-0898-3.

Poland, M. P. (2014), Time-averaged discharge rate of subaerial lava at Kilauea Volcano, Hawai'i, measured from TanDEM-X interferometry: Implications for magma supply and storage during 2011-2013, *Journal of Geophysical Research-Solid Earth*, *119*(7), 5464–5481, doi:10.1002/2014jb011132.

Poland, M. P., A. Miklius, A. J. Sutton, and C. R. Thornber (2012), A mantle-driven surge in magma supply to Kilauea Volcano during 2003-2007, *Nature Geoscience*, *5*(4), 295–U97, doi:10.1038/ngeo1426.

Poland, M. P., A. Miklius, and E. K. Montgomery-Brown (2014), Magma supply, storage, and transport at shield-stage Hawaiian volcanoes: Chapter 5 in Characteristics of Hawaiian volcanoes, in *Characteristics of Hawaiian volcanoes*, vol. 1801, edited by M. P. Poland, T. J. Takahashi, and C. M. Landowski, pp. 179–234, U.S. Geological Survey Professional Paper, Reston, VA, doi:10.3133/pp18015.

Pritchard, M. E., and M. Simons (2004), An InSAR-based survey of volcanic deformation in the southern Andes, *Geophysical Research Letters*, *31*(15), 4, doi:10.1029/2004gl020545.

Pritchard, M. E., J. A. Jay, F. Aron, S. T. Henderson, and L. E. Lara (2013), Subsidence at southern Andes volcanoes induced by the 2010 Maule, Chile earthquake, *Nature Geoscience*, *6*(8), 632–636, doi:10.1038/ngeo1855.

Pritchard, M. E., J. Biggs, C. Wauthier, E. Sansosti, D. W. Arnold, F. Delgado, S. K. Ebmeier, S. T. Henderson, K. Stephens, C. Cooper, K. Wnuk, F. Amelung, V. Aguilar, P. Mothes, O. Macedo, L. E. Lara, M. P. Poland, and S. Zoffoli (2018), Towards coordinated regional multi-satellite InSAR volcano observations: results from the Latin America pilot project, *Journal of Applied Volcanology*, doi:10.1186/s13617-018-0074-0.

Pritchard, M. E., T. A. Mather, S. R. McNutt, F. J. Delgado, and K. Reath (2019), Thoughts on the criteria to determine the origin of volcanic unrest as magmatic or non-magmatic, *Philosophical Transactions of the Royal Society A: Mathematical, Physical and Engineering Sciences*, *377*(2139), 20180,008, doi:10.1098/rsta.2018.0008.

Reath, K., M. Pritchard, M. Poland, F. Delgado, S. Carn, D. Coppola, B. Andrews, S. K. Ebmeier, E. Rumpf, S. Henderson, S. Baker, P. Lundgren, R. Wright, J. Biggs, T. Lopez, C. Wauthier, S. Moruzzi, A. Alcott, R. Wessels, J. Griswold, S. Ogburn, S. Loughlin, F. Meyer, G. Vaughan, and M. Bagnardi (2019), Thermal, Deformation, and Degassing Remote Sensing Time Series (CE 2000-2017) at the 47 most Active Volcanoes in Latin America: Implications for Volcanic Systems, *Journal of Geophysical Research: Solid Earth*, doi:10.1029/2018JB016199.

Remy, D., Y. Chen, J. L. Froger, S. Bonvalot, L. Cordoba, and J. Fustos (2015), Revised interpretation of recent InSAR signals observed at Llaima volcano (Chile), *Geophysical Research Letters*, *42*(10), 3870–3879, doi:10.1002/2015gl063872.

Reverso, T., J. Vandemeulebrouck, F. Jouanne, V. Pinel, T. Villemin, E. Sturkell, and P. Bascou (2014), A two-magma chamber model as a source of deformation at Grimsvotn Volcano, Iceland, *Journal of Geophysical Research-Solid Earth*, *119*(6), 4666–4683, doi:10.1002/2013jb010569.

Romero, J., F. Aguilera, F. Delgado, D. Guzmán, A. R. Van Eaton, N. Luego, J. Caro, J. Bustillos, A. Guevara, S. Holbik, D. Tormey, and Z. I. (2020), Combining ash analyses with remote sensing to identify juvenile magma involvement and fragmentation mechanisms during the 2018/19 small eruption of Peteroa volcano (Southern Andes), *Journal of Volcanology and Geothermal Research*, *402*, doi:10.1016/j.jvolgeores.2020.106984.

Rosen, P. A., S. Hensley, G. Peltzer, and M. Simons (2004), Updated repeat orbit interferometry package released, *Eos, Transactions American Geophysical Union*, *85*(5), 47, doi:10.1029/2004EO050004.

Rosen, P. A., E. Gurrola, G. F. Sacco, and H. Zebker (2012), The InSAR Scientific Computing Environment.

Sansosti, E., P. Berardino, M. Manunta, F. Serafino, and G. Fornaro (2006), Geometrical SAR image registration, *Ieee Transactions on Geoscience and Remote Sensing*, *44*(10), 2861–2870, doi:10.1109/tgrs.2006.875787.

Schipper, C. I., J. M. Castro, H. Tuffen, M. R. James, and P. How (2013), Shallow vent architecture during hybrid explosive-effusive activity at Cordon Caulle (Chile, 2011-12): Evidence from direct observations and pyroclast textures, *Journal of Volcanology and Geothermal Research*, *262*, 25–37, doi:10.1016/j.jvolgeores.2013.06.005.

Segall, P. (2010), *Earthquake and volcano deformation*, 432 pp., Princeton University Press, Princeton.

Sepulveda, F., K. Dorsch, A. Lahsen, S. Bender, and C. Palacios (2004), Chemical and isotopic composition of geothermal discharges from the Puyehue-Cordon Caulle area (40.5 degrees S), Southern Chile, *Geothermics*, *33*(5), 655–673, doi:10.1016/j.geothermics.2003.10.005.

Sepulveda, F., A. Lahsen, S. Bonvalot, J. Cembrano, A. Alvarado, and P. Letelier (2005), Morphostructural evolution of the Cordon Caulle geothermal region, Southern Volcanic Zone, Chile: Insights from gravity and Ar-40/Ar-39 dating, *Journal of Volcanology and Geothermal Research*, *148*(1-2), 165–189, doi:10.1016/j.jvolgeores.2005.03.020.

Sepulveda, F., A. Lahsen, and T. Powell (2007), Gas geochemistry of the Cordon Caulle geothermal system, Southem Chile, *Geothermics*, *36*(5), 389–420, doi:10.1016/j.geothermics.2007.05.001.

Sigmundsson, F., S. Hreinsdottir, A. Hooper, T. Arnadottir, R. Pedersen, M. J. Roberts, N. Oskarsson, A. Auriac, J. Decriem, P. Einarsson, H. Geirsson, M. Hensch, B. G. Ofeigsson, E. Sturkell, H. Sveinbjornsson, and K. L. Feigl (2010), Intrusion triggering of the 2010 Eyjafjallajokull explosive eruption, *Nature*, *468*(7322), 426–U253, doi:10.1038/nature09558.

Sigmundsson, F., M. Parks, R. Pedersen, K. Jonsdottir, B. G. Ofeigsson, R. Grapenthin, S. Dumont, P. Einarsson, V. Drouin, E. R. Heimisson, A. R. Hjartardottir, M. Gumundsson, H. Geirsson, S. Hreinsdottir, E. Sturkell, E. Hooper, . Hognadottir, K. Vogfjor, T. Barnie, and M. J. Roberts (2018), Magma Movements in Volcanic Plumbing Systems and their Associated Ground Deformation and Seismic Patterns, in *Volcanic and Igneous Plumbing Systems : Understanding Magma Transport, Storage, and Evolution in the Earth's Crust*, edited by S. Burchardt, chap. 11, pp. 285–322, Elsevier, doi:10.1016/B978-0-12-809749-6.00011-X.

Sigmundsson, F., V. Pinel, R. Grapenthin, A. Hooper, S. A. Halldórsson, P. Einarsson, B. G. Ófeigsson, E. R. Heimisson, K. Jónsdóttir, M. T. Gudmundsson, K. Vogfjörd, M. Parks, S. Li, V. Drouin, H. Geirsson, S. Dumont, H. M. Fridriksdottir, G. B. Gudmundsson, T. J. Wright, and T. Yamasaki (2020), Unexpected large eruptions from buoyant magma bodies within viscoelastic crust, *Nature Communications*, *11*(1), 2403, doi:10.1038/s41467-020-16054-6.

Singer, B. S., B. R. Jicha, M. A. Harper, J. A. Naranjo, L. E. Lara, and H. Moreno-Roa (2008), Eruptive history, geochronology, and magmatic evolution of the Puyehue-Cordon Caulle volcanic complex, Chile, *Geological Society of America Bulletin*, *120*(5-6), 599–618, doi:10.1130/b26276.1.

Sparks, R. S. J., and K. V. Cashman (2017), Dynamic Magma Systems: Implications for Forecasting Volcanic Activity, *Elements*, *13*(1), 35–40, doi:10.2113/gselements.13.1.35.

Sparks, R. S. J., J. Biggs, and J. W. Neuberg (2012), Monitoring Volcanoes, *Science*, *335*(6074), 1310–1311, doi:10.1126/science.1219485.

Sparks, R. S. J., C. Annen, J. D. Blundy, K. V. Cashman, A. C. Rust, and M. D. Jackson (2019), Formation and dynamics of magma reservoirs, *Philosophical Transactions of the Royal Society A: Mathematical, Physical and Engineering Sciences*, *377*(2139), 20180,019, doi:10.1098/rsta.2018.0019.

Stern, C. R. (2004), Active Andean volcanism: its geologic and tectonic setting, *Revista Geologica De Chile*, *31*(2), 161–206.

Tait, S., and B. Taisne (2012), The dynamics of dike propagation, in *Modeling Volcanic Processes The Physics and Mathematics of Volcanism*, edited by S. A. Fagents, T. K. P. Gregg, and R. M. C. Lopes, pp. 32–54, Cambridge University Press.

Tait, S., C. Jaupart, and S. Vergniolle (1989), Pressure, gas content and eruption periodicity of a shallow, crystallizing magma chamber, *Earth and Planetary Science Letters*, *92*(1), 107–123, doi:10.1016/0012-821x(89)90025-3.

Thelen, W. A., A. Miklius, and C. Neal (2017), Volcanic unrest at Mauna Loa, Earth's largest active volcano, *EOS*, *98*, doi:doi.org/10.1029/2017EO083937.

Tizzani, P., M. Battaglia, R. Castaldo, A. Pepe, G. Zeni, and R. Lanari (2015), Magma and fluid migration at Yellowstone Caldera in the last three decades inferred from InSAR, leveling, and gravity measurements, *Journal of Geophysical Research-Solid Earth*, *120*(4), 2627–2647, doi:10.1002/2014jb011502.

Townsend, M., and C. Huber (2020), A critical magma chamber size for volcanic eruptions, *Geology*, doi:10.1130/G47045.1.

Tuffen, H., M. R. James, J. M. Castro, and C. I. Schipper (2013), Exceptional mobility of an advancing rhyolitic obsidian flow at Cordon Caulle volcano in Chile, *Nature Communications*, *4*, 7, doi:10.1038/ncomms3709.

Velez, M. L., P. Euillades, A. Caselli, M. Blanco, and J. Martinez Diaz (2011), Deformation of Copahue volcano: Inversion of InSAR data using a genetic algorithm, *Journal of Volcanology and Geothermal Research*, *202*(1-2), 117–126, doi:10.1016/j.jvolgeores.2011.01.012.

Velez, M. L., P. Euillades, M. Blanco, and L. Euillades (2015), Ground Deformation Between 2002 and 2013 from InSAR Observations, in *Copahue Volcano*, edited by F. Tassi, O. Vaselli, and A. T. Caselli, Active Volcanoes of the World, p. 293, Springer-Verlag Berlin Heidelberg, doi:10.1007/978-3-662-48005-2.

Walwer, D., M. Ghil, and E. Calais (2019), Oscillatory nature of the Okmok volcano's deformation, *Earth and Planetary Science Letters*, doi:10.1016/j.epsl.2018.10.033.

Wendt, A., A. Tassara, J. C. Baez, D. Basualto, L. E. Lara, and F. García (2017), Possible structural control on the 2011 eruption of Puyehue-Cordon Caulle Volcanic Complex (southern Chile) determined by InSAR, GPS and seismicity, *Geophysical Journal International*, *208*(1), 134–147, doi:10.1093/gji/ggw355.

Wessel, P., and W. H. F. Smith (1998), New, improved version of generic mapping tools released, *Eos, Transactions American Geophysical Union*, *79*(47), 579, doi:10.1029/98EO00426.

Wicks, C., J. C. de la Llera, L. E. Lara, and J. Lowenstern (2011), The role of dyking and fault control in the rapid onset of eruption at Chaiten volcano, Chile, *Nature*, *478*(7369), 374–+, doi:10.1038/nature10541.

Wilson, C. J. N. (2017), Volcanoes: Characteristics, Tipping Points, and those Pesky Unknown Unknowns, *Elements*, *13*(1), 41–46, doi:10.2113/gselements.13.1.41.

Wilson, L., R. S. J. Sparks, and G. P. L. Walker (1980), Explosive volcanic eruptions - IV. The control of magma properties and conduit geometry on eruption column behaviour, *Geophysical Journal of the Royal Astronomical Society*, *63*(1), 117–148, doi:10.1111/j.1365-246X.1980.tb02613.x.

Wong, Y., and P. Segall (2019), Numerical analysis of time-dependent conduit magma flow in dome-forming eruptions with application to Mount St. Helens 2004-2008, *Journal of Geophysical Research: Solid Earth*, doi:10.1029/2019jb017585.

Yunjun, Z., H. Fattahi, and F. Amelung (2019), Small baseline InSAR time series analysis: Unwrapping error correction and noise reduction, doi:10.1016/j.cageo.2019.104331.

Zebker, H. A., S. Hensley, P. Shanker, and C. Wortham (2010), Geodetically Accurate InSAR Data Processor, *Ieee Transactions on Geoscience and Remote Sensing*, *48*(12), 4309–4321, doi:10.1109/tgrs.2010.2051333.

Zhan, Y., P. M. Gregg, H. Le Mével, C. A. Miller, and C. Cardona (2019), Integrating Reservoir Dynamics, Crustal Stress, and Geophysical Observations of the Laguna del Maule Magmatic System by FEM Models and Data Assimilation, *Journal of Geophysical Research: Solid Earth*, *n/a*(n/a), doi:10.1029/2019JB018681.